Development of a Synthesis of Quantum-Confined, Wurtzite $CuInS_2$ Nanoparticles

By

Bryson Charles Howard

Thesis

Submitted to the Faculty of the

Graduate School of Vanderbilt University

in partial fulfillment of the requirements

for the degree of

MASTER OF SCIENCE

in

Chemistry

August, 2014

Nashville, Tennessee

Approved:

Janet E. Macdonald, Ph.D.

Timothy P. Hanusa, Ph.D.

CHEMISTRY

Development of a Synthesis of Quantum-Confined, Wurtzite $CuInS_2$ Nanoparticles

Bryson Charles Howard

Thesis under the direction of Assistant Professor Janet E. Macdonald

$CuInS_2$ is a ternary semiconductor material with potential alternative energy applications in photovoltaic devices and in systems designed for photocatalytic water reduction. To date, the majority of research into $CuInS_2$ nanoparticles has focused on those that possess the thermodynamically favored chalcopyrite crystal structure. Wurtzite, the kinetically favored crystal structure, is exclusively seen in nano-structures, and has been significantly less studied. The synthesis of "large" wurtzite $CuInS_2$ nano-disks has already been established, but the particles show energetic imperfections. This study details the development of a synthesis that produces sub-4 nm, quantum-confined, wurtzite $CuInS_2$ nanoparticles that show emission near the band gap, a unique observation for wurtzite $CuInS_2$. The particles are produced using a hot-injection method using metal salts as precursors. The structure and properties of these particles were detailed via absorbance and fluorescence spectroscopy, transmission electron microscopy, powder X-Ray diffraction, and inductively coupled plasma optical emission spectroscopy. Attempts were then made to develop a modified synthesis by which the band gap and size of the particles could be controllably manipulated. These efforts culminated in the addition of oleic acid to the reaction mixture, which showed promising initial results. Continued investigation into these quantum-confined wurtzite $CuInS_2$ particles revealed some of the inherent inconsistencies

of the synthesis developed in this study. The future work of this project will focus on understanding and explaining the apparent variability in the properties of the particles produced by this synthesis.

Approved:

Janet E. Macdonald, Ph.D.

To my family for their support, calmness, and perspective

and

To my friends for their unending quips, open ears, and, hopefully, love
Merci bien

ACKNOWLEDGMENTS

Without the financial support of the Vanderbilt University Department of Chemistry, the Vanderbilt Institute of Nanoscale Science and Engineering, TN-SCORE, and the Waite Philip Fishel Endowment Fund, none of the work presented in this thesis would have been possible.

I have had the pleasure of working with a number of extremely helpful, bright, and skilled scientists throughout my time with this project. I am very much indebted to the assistance and collaboration that I received from my predecessor and descendent on this project, Dr. Emil Hernández-Pagan and Alice Leach, respectively. I would also like to thank Dr. Xiao Shen for performing the effective mass calculations. I am especially grateful to my advisor during my time at Vanderbilt, Dr. Janet Macdonald. You have inspired me and pushed me to always aim higher. You have taught me a very great deal about myself and about science, and you have shown me what it is to be a truly exemplary scientist. I am forever thankful for your patience.

My sincerest thanks go to my family, who has supported me throughout. Much of this would have been impossible without your guidance. My warmest thanks go to my friends who have listened to me with tolerance. Surely, none of this would have been possible if not for your fervent prodding and optimism.

TABLE OF CONTENTS

LIST OF TABLES

LIST OF FIGURES

CHAPTER I

INTRODUCTION

In recent decades, nanotechnology has grown to encompass a wide breadth of interests and expertise. Nanoparticle research, in particular, has facilitated dramatic achievements in material[1,2,3], biomedical[4,5,6,7], and photovoltaic applications[8,9,10]. Nanoparticles are increasingly employed in developing emerging photovoltaic applications for solar-based renewable energy sources as an answer to the present energy dilemma facing our planet. Continuing global industrialization has led to rapidly increasing energy demands, which far outpace traditional energy sources and produce unsustainable environmental pressures with dire consequences if left unchecked.[11] It is imperative that alternative energy sources be developed that boast both impressive efficiencies and relatively mild environmental impacts, and it is in that vein that this research is motivated.[12]

Nanotechnology has opened the door for numerous advances in alternative energy research. Semiconductor nanoparticles, called quantum dots, are attractive light absorbing materials for solar energy capture. They have been applied in photovoltaic devices and to the photocatalytic production of clean-burning, renewable hydrogen gas.[8] There are two main designs using quantum dots for the solar-production of hydrogen gas. In the first case, the splitting of water happens directly on the quantum dot surface or on an attached catalytic domain. In the second, quantum dots are used as the photo-absorber layer in a photovoltaic device which is connected to external electrodes for water electrolysis.

The exploitation of the unique optical and chemical properties of nanoparticles is not new. Since antiquity, numerous societies have unknowingly employed nanoparticles in various aspects of their lives. In ancient Egypt, a recipe was followed for hair-dyeing wherein the subsequent darkening of the hair was a result of the formation of PbS nanocrystals.[13] Craftsmen too made use of the unique properties of nanostructures without being fully aware. Stained glass pieces were valued for their vibrant reds and violets, which resulted from the surface plasmon of gold nanoparticles that had been embedded in the glass.[14] Arabic craftsmen as early as the ninth century developed glazes for ceramic pottery with a distinctive luster coming from what were later found to be metallic nanoparticles that nucleated from metal salts that were heated in the reducing environment of a kiln.[15] More recently, silver nanoparticles have been used in bandages and clothing for their antimicrobial effects.[16] Throughout history nanoparticles have found uses in society, and only recently have nanostructures been expressly designed for specific applications.

The increasing interest in nanochemistry stems primarily from the unique physical and chemical properties that are characteristic to materials on the nano-scale compared to their bulk counterparts, which allows for heightened functionality. The increased surface area to volume ratio of the particles allows for increased reaction rates of surface mediated reactions, lower melting points, and even stabilization of metastable crystalline phases not readily seen in the bulk. Bulk gold, for instance, is valued in part because of its chemical inertness, but when formed into nanoparticles, gold shows noted catalytic activity for the oxidation of several molecules, including carbon monoxide.[17]

This study focuses on the unique opto-electronic properties and possible uses of quantum dots. Quantum dots can be produced using solution-based chemistry that can boast mild synthetic

conditions.[18] They also possess size-tunable band gaps. By decreasing the size of a quantum dot, the band gap energy will increase.[19] This trait is useful for photocatalytic applications because the band gap energy can be tailored to match the solar spectrum and to the potential of an attached material or to the electrochemical potential of a solution reaction to facilitate photo-induced charge transfer.

The research described herein details the efforts to produce particles of $CuInS_2$ with desirable characteristics for possible employment in photocatalytic or photovoltaic systems, with a particular emphasis on the reaction conditions that control the opto-electronic properties of the quantum dots.

Quantum Dot Photocatalytic Systems

Quantum dots are a powerful tool for the photocatalytic reduction of water to produce hydrogen gas, a clean-burning and renewable fuel source.[20] Hybrid systems coupling a semiconductor nanoparticle of appropriate energetic properties with a catalytic metal domain have demonstrated the ability to photocatalytically reduce water to give hydrogen gas in the

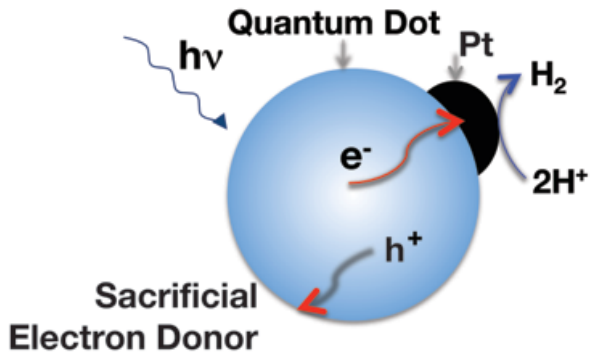

Figure 1. Diagram of Generic Quantum Dot System for Photocatalytic Reduction of Water

presence of a sacrificial reductant, as can be seen in Figure 1.[21] Photocatalytic water reduction has been shown using a variety of semiconductor materials including ZnS[22], CdSe[23,24], $AgInS_2$[25], and $CuInS_2$.[26,27]

The energetic and optical properties of both the semiconductor nanoparticle and the metal domain are key to the function of these hybrid nanoparticles as a photocatalyst for water-reduction. The semiconductor domain, when exposed to a photon of sufficient energy, can produce an electron-hole pair, where the electron is excited into the conduction band, while the hole remains in the valence band of the material. The energy necessary to form this exciton pair is dictated by the band energies intrinsic to a given material.[28] If the gap between the valence and conduction bands straddles the electrochemical potentials necessary to reduce water to hydrogen gas, then the particular semiconductor material is a viable candidate for use in a quantum dot photocatalytic system for hydrogen gas production.

These two-component systems also utilize a noble metal domain, such as gold or platinum, which acts as an electron syphon. The Fermi level of the metal sits below the conduction band of the semiconductor. This means that once an electron has been excited into the conduction band of the semiconductor, it can transfer to the metal domain in a facile manner. Platinum is particularly effective at this electron sequestration. Electrons are able to diffuse from the semiconductor to the metal in less than 1.0 ps, and there is negligible build up of electrons in the quantum dot.[29] Following charge separation, the electrons can reduce water to hydrogen gas on the catalytically active surface of the metallic domain.

Another application of quantum dots in photovoltaic devices is in Quantum Dot Sensitized Solar Cells (QDSSCs). A typical solar cell requires a semiconductor material that can absorb light. The nanoparticles sit at the interface between two materials of differing electronic

or electrochemical properties that facilitate charge separation and extraction. These systems take advantage of the high absorption coefficients of quantum dots as the light-gathering portion of the solar cell, and require only thin photo-absorber layers.[30,31] Additionally, these quantum dot sensitized systems can be tuned to perform a wide variety of photocatalytic reactions.[32,33]

With the growing emphasis on environmentalism and sustainability, interest is increasingly being focused on developing and understanding semiconductor materials that are non-toxic, stable, and widely-applicable for many uses. The research detailed in this project is aimed toward that pursuit and the further characterization and understanding of the intricacies of wurtzite $CuInS_2$.

$CuInS_2$ – Candidate Semiconductor Material

Since the first development of hybrid quantum dot photocatalytic systems, the materials most heavily investigated as the semiconductor domain have been the cadmium chalcogenides (namely CdS and CdSe), TiO_2[34], ZnO[29], and PbS.[8] These materials have a number of positive characteristics, including favorable band gap energies, high molar absorptivities due to their direct band gaps, and their optoelectronic properties and surface chemistries are well studied.[35,36,37] They are each, however, burdened by some negative properties. For instance, TiO_2 and ZnO both have very large band gaps, which require high energy light in order to form an exciton pair, missing out on much of the solar spectrum. The cadmium chalcogenides and PbS present a health concern because of the high toxicity of cadmium and lead[38], and they suffer from the relatively low abundance of cadmium and the heavier chalcogenides.

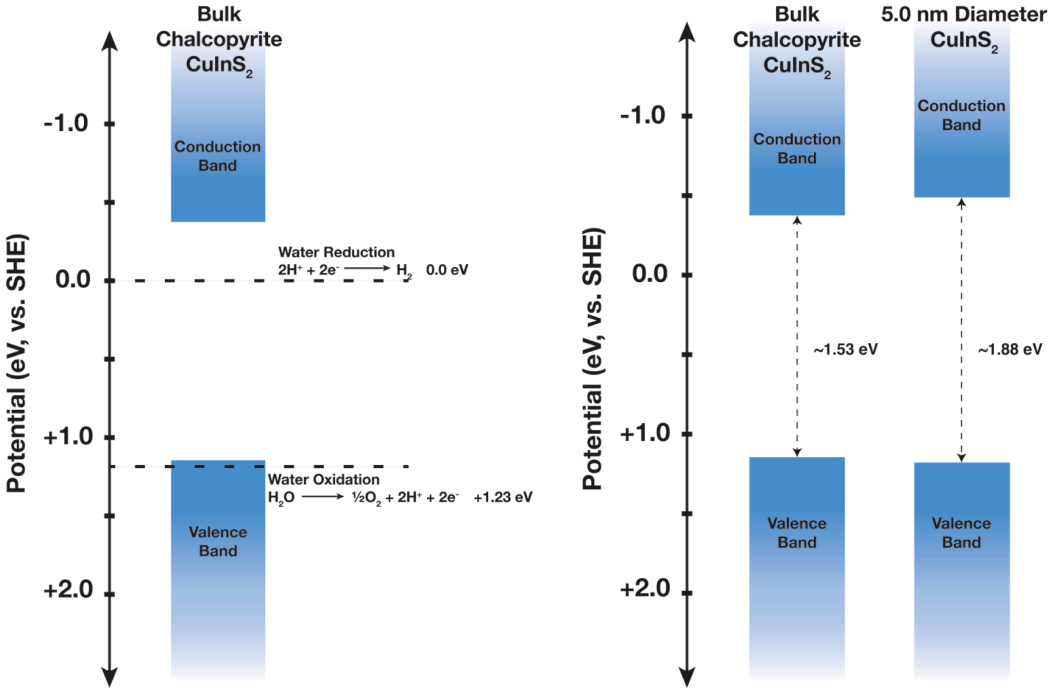

Figure 2. Band Potentials of Bulk and 5.0 nm Quantum-Confined $CuInS_2$

$CuInS_2$ has been presented as a viable replacement semiconductor material.[39] $CuInS_2$ enjoys many of the same advantageous characteristics as the cadmium chalcogenides but it also improves upon the notable disadvantages that limit those materials. $CuInS_2$ has a direct band gap, which results in a high molar absorptivity, 5.0×10^5 cm^{-1} for the chalcopyrite stucture[40], making the material an efficient photo-absorber.[41,40] This means that a large portion of incident photons can be absorbed and used to form an exciton pair. Furthermore, the band gap energy of bulk chalcopyrite $CuInS_2$ is ~1.53 eV,[42] which allows the material to absorb the broadband visible light emission of sunlight.

Additionally, the conduction and valence bands of $CuInS_2$ are situated favorably relative to the reduction potential necessary to produce hydrogen gas from water. The energy of the conduction and valence bands are approximately -0.34 eV and 1.16 eV relative to the Standard

Hydrogen Electrode (SHE), respectively,[43] which straddle the electrochemical potential required for water reduction. If $CuInS_2$ nanoparticles can be quantum-confined, it is reasonable to expect the valence band to decrease in energy below the threshold needed to perform water oxidation. The energy of the valence and conduction bands of a semiconductor can be shifted according to the quantum-confinement effects calculated using the effective masses of the hole and the electron for the material, *vide infra*. The calculated expansion of the band gap for 5.0 nm diameter $CuInS_2$ nanoparticles is shown in Figure 2, and it can be seen that quantum-confinement can shift the valence band energy below the oxidation potential of water. Thus, it may be possible to employ $CuInS_2$ as the semiconducting material in complete water-splitting systems.

$CuInS_2$ is also a material of interest for photocatalytic alternative energy production because it improves upon some of the shortcomings of traditionally used semiconductors. Silicon has been the most common photovoltaic absorber material, but it is an indirect band gap semiconductor.[44] This means that the absorption of a photon must be coincident with a change in momentum, in the form of a coupling with a phonon. This low probability transition results in a small absorption coefficient and limits the ability of silicon to make use of large amounts of incident light without very thick layers. Because of this quality, very large and pristine silicon crystals are a requirement, and the process by which such crystals are produced is expensive and delicate. The direct band gap and consequent high molar absorptivity of $CuInS_2$ will allow for a much thinner light-absorbing layer in a photovoltaic device.

$CuInS_2$ avoids the use of highly toxic cadmium, the component elements are relatively more abundant[45], and it exhibits improved photostability over the cadmium chalcogenides. Furthermore, $CuInS_2$ improves on a very notable shortcoming of two of the earliest developed

solar photocatalysts for water splitting – TiO_2 and ZnO. Their band gaps are 3.0 eV[46] and 3.37 eV[47], respectively, and thus only absorb light in the ultraviolet region, missing out on the most abundant portion of the sun's radiation, which is visible light. The bulk band gap of $CuInS_2$, however, is 1.53 eV, which corresponds to a minimum wavelength of light of ~810 nm. This means that $CuInS_2$ will form an exciton pair under exposure to visible light, and will thus more efficiently make use of the solar spectrum.

$CuInS_2$ quantum dots are of interest for alternative energy applications, but because this material is relatively new, it lacks the comprehensive understanding that the more established quantum dot materials already enjoy. Bulk $CuInS_2$ has been studied for some time for use in photovoltaic devices[41,48], but only recently has attention shifted toward the use of nanoscale $CuInS_2$.[39,47] $CuInS_2$ is the ternary derivative of the binary ZnS material, thus it exists in the same crystal stuctures as that material, with cubic and hexagonal polymorphs.[49] These crystal structures are derived by substituting copper and indium into the cation positions that would be filled by zinc. The crystal structures observed in $CuInS_2$ are zinc blende, chalcopyrite, and wurtzite. The zinc blende structure is tetragonal, and the chalcopyrite structure is nearly cubic in nature. They are largely identical structures, but they vary by the fact that the cations (Cu^+ and In^{3+}) are disordered in zinc blende but ordered in chalcopyrite.[49] There is also a slight difference in the unit cell dimensions between the two. The chalcopyrite structure is what has been predominantly observed in the bulk material. There exists also the less common wurtzite crystal structure, which is hexagonal in nature. This structure is rarely seen in the bulk material, but nanoparticle syntheses have been developed that can preferentially produce this structure.[50]

Nanoparticles of both chalcopyrite and wurtzite structure have been produced, and to-date chalcopyrite particles have received the highest amount of investigation. Reliable

syntheses have been developed to create quantum-confined chalcopyrite nanoparticles of various sizes, and those structures have found applications in photovoltaic devices.[51] The fluorescence of the particles with this crystal structure has been determined to result from donor-acceptor pair recombination, not from band gap emission. The emission is Stokes shifted by ~50 meV to lower energy relative to the band gap absorbance.[18] The fluorescence depends on the copper defects present in the crystals, and quantum yields have been reported up to 70%, when the density of copper vacancies is high.[52,53] It is anticipated that wurtzite $CuInS_2$ nanoparticles would have similar opto-electronic properties as the chalcopyrite particles; this supposition is one of the aims of this study.

Wurtzite $CuInS_2$ possesses all of the same attractive properties of the chalcopyrite material, and its bulk band gap has been calculated to be ~0.05 eV lower in energy than that of chalcopyrite $CuInS_2$.[54] Thus the band gap of wurtzite $CuInS_2$ is also situated perfectly for efficient absorbance of the solar spectrum. But the wurtzite structure is unique from chalcopyrite because of its anisotropic nature. The anisotropic crystal structure (Figure 3) allows for the possibility to grow asymmetric nanostructures, such as rods or disks. Asymmetric morphologies

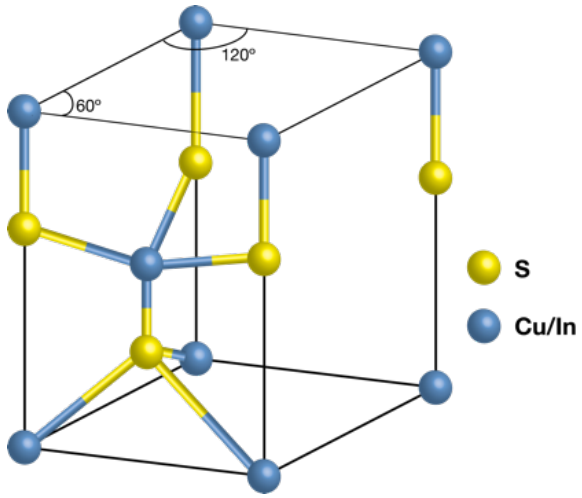

Figure 3. Crystal Structure of Wurtzite $CuInS_2$

allow for particles that can act as light-absorbing antennae, and they can permit orthogonal charge carrier conductivity. This means that the electrons and holes can travel perpendicularly to one another, which is advantageous for hybrid nanoparticle photocatalytic systems.[55,56] Additionally, it has been previously reported that the wurtzite crystal structure lacked any ordering among the cations (Cu^{+} and In^{3+}), similar to the zinc blende structure.[57] Recent work rom our lab shows that the copper and indium cations are, in fact, ordered in wurtzite $CuInS_2$, and that there is a family of possible phases all with different orderings.[54]

A synthesis for large nano-disks of wurtzite $CuInS_2$ has been produced, and these particles show a significant Stokes shift in photoluminescence of ~0.25 eV, *vide infra*. It is hypothesized that the development of a synthesis of dramatically smaller particles would improve the optical efficiency of the material and reduce the magnitude of the Stokes shift. As the push toward sustainability and viable alternative fuel sources grows ever stronger, $CuInS_2$ presents itself as a next step in the progression of useful semiconductor materials. The main drawback of the material is that it is not yet as thoroughly understood as the more traditional materials. This study represents an effort to characterize and better understand $CuInS_2$ nanoparticles for their future use in photocatalytic and photovoltaic devices.

Quantum-Confinement and Effective Masses of Hole and Electron

Quantum-confinement is an effect that is observed in quantum dots that are smaller than the Bohr exciton radius of the given semiconductor, by which the band gap energy of the particle is a function of the particle diameter. The amount of expansion in the band gap is dependent on the effective masses of the hole and the electron for the material. The effective masses

(m_h^* and m_e^*) for chalcopyrite $CuInS_2$ are reported in the literature to be 1.30 m_0 for the hole and 0.16 m_0 for the electron[58], but they have not been reported for wurtzite $CuInS_2$. In order to apply quantum-confinement calculations to these wurtzite particles, it was important to have the relevant effective masses.

Our collaborator, Dr. Xiao Shen of the Vanderbilt University Physics Department and the research group of Professor Sokrates Pantelides, performed calculations in order to determine the effective masses of the hole and the electron for wurtzite $CuInS_2$.[59] The electron and hole effective masses (m_e^* and m_h^*) of four wurtzite-derived phases of $CuInS_2$, along with that of the chalcopyrite phase, were calculated through hybrid density functional theory (DFT). The parameters of the semi-empirical calculation were modified to reproduce the experimental band gap of the chalcopyrite phase of $CuInS_2$ (1.53 eV).[60] The parameters from this calculation aided Dr. Shen in the calculations related to the wurtzite phase.

For all the $CuInS_2$ phases, a single electron band exists at the conduction band minimum (CBM), while three hole bands, very close in energy, appear near the valence band maximum for each phase. The valence band maxima are denoted in Table 1 by their energy difference compared to the highest valence band maxima, and they will furthermore be generally annotated VBM, VBM-1, and VBM-2. The calculated m_e^* and m_h^* values are listed in Table 1. For all the phases, the three m_e values are nearly isotropic while the m_h values show large anisotropy. As a validation of the theory, the calculated value of m_e^* for chalcopyrite $CuInS_2$ is 0.15, which agrees well with the experiment value of 0.16;[48] meanwhile the calculated m_h^* values range from 0.23 to 0.52, along with two values near 1.3 for the VBM-1 band in x and z-directions (for the definition of the directions, see the caption of Table I). These values agree with the experimental values of 1.3, 1.28, 1.20, and 0.40.[48, 61] According to Table 1, for all four wurtzite-derived

phases, in the z-direction, the m_h^* value ranges from 1.3 to 1.6 for VBM and VBM-1 bands, while it equals 0.15 for the VBM-2 band.

Table 1. Effective masses of the electrons and holes as a fraction of m_0. (The x, y, z directions of chalcopyrite phase refer to the directions in the hexagonal representation, which correspond to the (11$\bar{2}$), (1$\bar{1}$0), and (111) planes of the underlying cubic lattice structure.)

			x	y	z
Chalcopyrite	m_e^*	CBM	0.15	0.15	0.15
	m_h^*	VBM	0.50	0.37	0.39
		VBM-0.022eV	1.3	0.52	1.3
		VBM-0.027eV	0.23	0.50	0.36
Wurtzite Phase 1	m_e^*	CBM	0.17	0.17	0.14
	m_h^*	VBM	0.21	1.1	1.3
		VBM-0.026eV	0.81	0.20	1.4
		VBM-0.090eV	1.4	1.3	0.15
Wurtzite Phase 2	m_e^*	CBM	0.16	0.17	0.15
	m_h^*	VBM	0.19	1.2	1.5
		VBM-0.046eV	1.0	0.19	1.6
		VBM-0.122eV	1.4	1.6	0.15
Wurtzite Phase 3	m_e^*	CBM	0.18	0.19	0.14
	m_h^*	VBM	0.33	0.41	1.4
		VBM-0.019eV	0.35	0.28	1.5
		VBM-0.096eV	1.4	1.4	0.15
Wurtzite Phase 4	m_e^*	CBM	0.17	0.17	0.14
	m_h^*	VBM	0.42	0.36	1.3
		VBM-0.024eV	0.27	0.32	1.3
		VBM-0.082eV	1.3	1.2	0.15

Using the m_e^* and m_h^* values calculated by Dr. Shen for wurtzite phase 2 in the z-direction[59] (boxed in Table 1) along with the Brus equation for quantum-confinement, the effect of a change in particle size on the band gap energy can be predicted. The z-direction values for effective masses were selected because they showed the least amount of variability between each phase. The varying effective masses across the three cardinal directions is a product of the anisotropic nature of the wurtzite structure, a unique characteristic in comparison

$$E_{gap}^{*} = E_{gap}^{bulk} + \frac{h^2}{8r^2}\left[\frac{1}{m_e^* m_o} + \frac{1}{m_h^* m_o}\right] - \frac{1.8e^2}{4\pi\varepsilon\varepsilon_0 r} \quad (1)$$

to the nearly cubic chalcopyrite structure. The Brus equation is represented in Equation 1, and it has been limited to the particle-in-a-box and Coulombic interaction terms, leaving out the polarization terms, which have relatively small effects on the band gap energy.[62] In this equation, r is the radius of the particles, m_0 is the mass of an electron, e is the charge of an electron, ε is the effective dielectric constant for $CuInS_2$, ε_0 is the permittivity of a vacuum, and E_{gap}^{bulk} is the bulk band gap of $CuInS_2$. For this study, it is assumed that the effective dielectric constant, a unitless value used to scale the permittivity of a vacuum, for wurtzite $CuInS_2$ is not significantly different from that of chalcopyrite $CuInS_2$, for which the value is 11.[58]

Equation 1 can be used to predict the band gap energy for a sample of particles with a known radius. When the equation is rearranged, it can also be used to predict the radius of a sample of nanoparticles based on an apparent band gap energy. The usefulness of this form of data analysis is discussed in more depth in Chapter IV.

The calculation of the effective masses of the hole and electron of wurtzite $CuInS_2$ by Dr. Shen also allowed for the determination of the Bohr exciton radius of wurtzite $CuInS_2$. The Bohr exciton radius of chalcopyrite $CuInS_2$ has been calculated in literature to be ~4.05 nm[58]. It was assumed that the calculated value for wurtzite $CuInS_2$ would be relatively similar. The Bohr exciton radius, r_B, can be calculated according to Equation 2.[63,64] In that equation, m_e^* is the

$$r_B = \left(\frac{\varepsilon_0}{\mu}\right) a_0 \;;\; \mu = \left[\frac{1}{(m_e^*)^{-1} + (m_h^*)^{-1}}\right] \quad (2)$$

effective mass of the electron of wurtzite $CuInS_2$, which is 0.15, and m_h^* is the effective mass of the hole, which is 1.5. In the equation, ε_0 is the dielectric constant of the material, which was again assumed to be similar to that of chalcopyrite $CuInS_2$, so a value of 11 was used. The hydrogen Bohr radius is represented by a_0, and it is 5.29×10^{-11} m. According to the values listed above, using Equation 2 calculates a value of 4.27 nm as the Bohr exciton radius for wurtzite $CuInS_2$. This radius is slightly larger than that of chalcopyrite $CuInS_2$, which means that quantum-confinement effects on the band gap of wurtzite particles should begin to be observed at slightly larger particle sizes than those for chalcopyrite particles.

Motivation For Study

Is the wurtzite crystal structure better suited for use in photocatalytic devices? Can one structure reliably produce advantageous particle morphologies? What unique opto-electronic characteristics might the wurtzite crystal structure exhibit? In order to answer these questions and others, a highly reproducible synthesis was used to form $CuInS_2$ nano-disks, which were known to be of the wurtzite crystal structure. Following these investigations, a synthesis procedure was developed that produces significantly smaller $CuInS_2$ nanoparticles. Studies were performed to elucidate the shape, size, crystal structure, and optical and electronic characteristics of these particles. Finally, efforts were made to adapt this synthesis to allow for modest tunability of the resultant particles – a challenge that proved to be unexpectedly complex.

CHAPTER II

SYNTHESIS AND CHARACTERIZATION OF $CuInS_2$ NANO-DISKS

Introduction

In the literature, there is a variety of research into $CuInS_2$ that has already been presented, ranging from studies of the bulk material to newer studies into the material on the nanoscale.[41,65,50] Within the past decade, focus has been placed on the synthesis of "nano-inks", or suspensions of $CuInS_2$ quantum dots, for use in photovoltaic and photocatalytic devices.[66] The research efforts focused on this material have led to the development of a number of applications for $CuInS_2$ nanoparticles in bioimaging[67,68] , photocatalysis[69,20] , and solar energy conversion[39,70] , but the majority of these advancements have the better-understood chalcopyrite crystal structure. A major goal of the work presented here was to increase the knowledge of the wurtzite crystal structure of $CuInS_2$.

The starting point for this work was to begin with an already developed synthesis that produced 14-20 nm $CuInS_2$ nano-disks with the desired wurtzite crystal structure[71]. The physical and opto-electronic properties of the particles synthesized by the procedure in this chapter were characterized using several techniques, and the results of that analysis helped to motivate much of the following work.

Experimental

For the synthesis of $CuInS_2$ nano-disks, a modified literature procedure was used in which CuCl and $InCl_3$ serve as the copper and indium sources and thiourea serves as the sulfur source.[71] This synthesis was performed under inert atmosphere (N_2) using standard Schlenk

Figure 4. Reaction Scheme for $CuInS_2$ Nano-Disks

techniques. In a typical reaction, CuCl (50.0 mg, 0.50 mmol), $InCl_3$ (111.0 mg, 0.50 mmol), thiourea (77.6 mg, 1.00 mmol), and 10.0 mL of oleylamine were added to a 25.0-mL reflux apparatus with a temperature probe. The temperature was set to 60 ºC, and the flask was placed under vacuum with stirring for at least 30 min. The reaction mixture began as a clear blue color and changed to a cloudy brown by the end of 30 min. The flask was then put under N_2 gas flow, and the temperature was increased to 245 ºC for 1 h. The reaction mixture was an opaque, inky black color. The reaction was stopped by removing the heating source and allowing the mixture to cool to below 40 ºC. A portion of unwashed product was diluted in hexanes in a quartz cuvette to collect optical spectra. The remainder of the product was thoroughly washed via precipitation by addition of ethanol followed by centrifugation for 5 min at 4400 rpm. The clear supernatant was decanted and the precipitate was resuspended in a solution of oleylamine in hexanes (1:100 by volume). This washing procedure was repeated at least three times until particles were

sufficiently isolated from excess solvent and ligands. A TEM grid was prepared of the product by diluting the sample in hexanes and drop casting the solution onto a carbon-coated nickel support grid. A general reaction scheme for this procedure can be seen in Figure 4.

Characterization

The product of this reaction was characterized by several means: absorbance spectroscopy, fluorescence spectroscopy, powder X-Ray Diffraction (XRD), and Transmission Electron Microscopy (TEM), and Selective Area Electron Diffraction (SAED). A JASCO V-670 Spectrophotometer was used to measure the absorbance spectra. A Jobin Yvon/Horiba Fluorolog-3 FL3-111 Spectrophotofluorometer was used to collect the fluorescence spectra with an excitation wavelength of 400 nm. XRD patterns were collected for these $CuInS_2$ nano-disks using a Scintag XGEN-4000 powder X-ray diffractometer with a Cu K_α X-Ray source ($\lambda = 1.541$ Å). Nanoparticle samples produced using this synthesis were analyzed via TEM using both a Philips CM-20 and a Tecnai Osiris Transmission Electron Microscope operating at working voltages of 200 keV. SAED images were collected using the Philips CM-20 instrument. The results of all of these characterization techniques can be seen in Figure 5. The absorbance spectrum seen in Figure 5 shows an absorption onset occuring very near to the band gap energy of bulk chalcopyrite $CuInS_2$, which is ~1.5 eV or a wavelength of ~825 nm. It is also similar to the calculated band gap of wurtzite $CuInS_2$, which has been estimated to be up to 80 meV lower in energy than that of chalcopyrite.[54] More recent calculations show the wurtzite band gap to be only 8.0 meV lower in energy. This result suggests that these nano-disks are large enough such that the particles do not exhibit any quantum-confinement effects. This claim is further

confirmed by the TEM image shown in Figure 5. In order for nanoparticles to be quantum-confined, the diamter of the particles must be smaller than the Bohr exciton radius of the material, which is calculated to be 4.27 nm for wurtzite $CuInS_2$. It is evident from the TEM image that the particles produced in this synthesis are significantly larger than the Bohr exciton radius, with diameters of 17.03 ± 1.31 nm; n =175 (average diameter ± standard deviation; n = number of particles measured). The average diameter from sample to sample can vary by as much as approximately 7 nm, but the standard deviations remain fairly consistent.

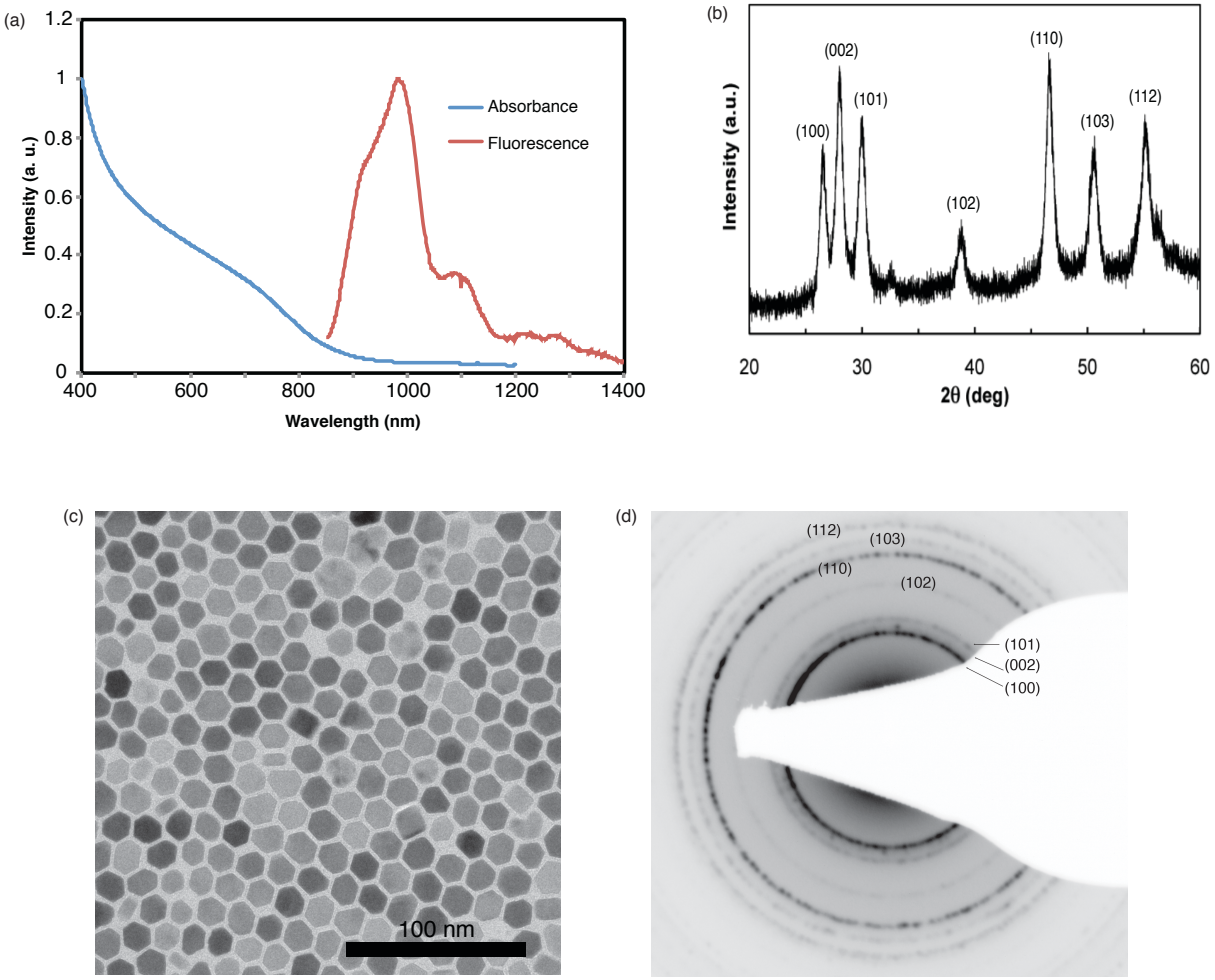

Figure 5. Characterization of $CuInS_2$ Nano-Disks. (a) Absorbance and Fluorescence, (b) Powder XRD indexed to wurtzite, (c) TEM image, and (d) SAED image indexed to wurtzite

It was previously mentioned that there are two common crystal structures for $CuInS_2$. Chalcopyrite is the cubic structure and it is the thermodynamically favored structure; it has been heavily studied for the bulk material. Wurtzite, the hexagonal structure, is the kinetic product and has only been seen in nanostructures and it is much less studied. The wurtzite crystal structure can be seen in Figure 3. The nanoparticles produced in this synthesis are hexagonally shaped, which can be seen in the TEM image in Figure 5, and this would suggest that their crystal structure is likely wurtzite. The XRD pattern for these particles confirms this identification, showing clearly defined reflection peaks that are indicative of the wurtzite crystal structure of $CuInS_2$.[72] The SAED image shows diffraction rings that further confirm the wurtzite structure, specifically the set of three rings very close to one another near the center of the diffraction pattern. This trio of rings is absent in the pattern of chalcopyrite $CuInS_2$.

The absorbance and fluorescence spectra also reveal some details about the atomic structure of these nanocrystals. As described earlier, the absorption onset occurs at a wavelength

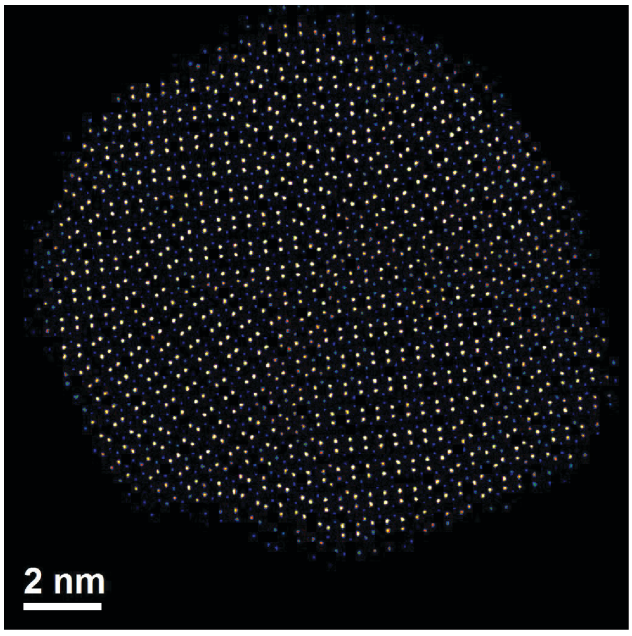

Figure 6. Aberration-Corrected STEM Annular Dark Field Image of $CuInS_2$ Nano-disk

around 825 nm, but the fluorescence spectrum shows peak emission at much longer wavelengths near 1000 nm. This is important because it shows that this material lacks band gap emission. We hypothesize that the absence of band gap emission is a result of the nano-disks having a multitude of defects and domain boundaries within the particles. Previous work shows that when these particles are viewed using aberration-corrected scanning transmission electron microscope (STEM) annular dark field (ADF) imaging, also known as Z-contrast imaging, there is evidence of twinning and domain boundaries, and the "seams" where different orientations of the wurtzite structure meet together may contain electronic defects and mid gap states. These crystal defects can be seen in Figure 6, a Z-contrast TEM image of a wurtzite $CuInS_2$ nano-disk synthesized according to this procedure.[54] In the wurtzite structure for $CuInS_2$, copper and indium can occupy the same sites, so it is possible to have points within the particle where there is an indium atom when there should be copper, or vice versa. These site defects could certainly provide a source of the observed lower energy fluorescence. The dramatic Stokes shift seen in the optical spectra of these nano-disks is indicative of a genre of defects possibly unique to wurtzite $CuInS_2$. The D-A pair fluorescence that is seen in chalcopyrite $CuInS_2$ typically shows a smaller red-shift in emission. Research into the emmission pathway favored by these wurtzite structures is an area of ongoing research in this group.

Conclusion

The modified literature procedure that was used to create $CuInS_2$ nano-disks produced particles that show the less common wurtzite crystal structure. The resultant particles absorb at a band gap energy that is similar to that of the bulk material, showing that the particles are too

large to be quantum-confined. Interestingly, they emit at wavelengths significantly longer than where they absorb. This dramatic Stokes shift likely results from low-energy trap state emission. We hypothesize that this emissive pathway is caused by defects at crystal phase boundaries.

It would be advantageous for several reasons to develop an adapted synthesis that would produce particles that maintain the wurtzite crystal structure and that are single-domain. Firstly, single-domain particles with diameters of approximately 5 nm would eliminate the phase boundaries observed in the larger nano-disks. It would, thus, be reasonable to anticipate that the particles would not contain the same number of crystal defects and trap states. By eliminating the defects within the crystal, it is expected that the magnitude of the emission through these pathways would be reduced, and other, higher energy pathways, such as band gap emission could become dominant. Finally, these single-domain particles would be small enough to experience effects of quantum-confinement. This is desirable because it would allow for a degree of tunability over the band gap energy of the particles, meaning that the energy of the exciton pair could be tailored for a variety of electrochemical reactions. This synthesis would be the first reported synthesis of quantum-confined, wurtzite $CuInS_2$ nanocrystals with band gap emission, and they could have potential uses in photocatalytic systems for water reduction.

CHAPTER III

SYNTHESIS AND CHARACTERIZATION OF QUANTUM-CONFINED, SINGLE-DOMAIN, WURTZITE $CuInS_2$ NANOCRYSTALS

Introduction

There are a number of distinct advantages that come from producing particles that are small enough to be quantum-confined. The band gap energy of quantum-confined semiconductor nanoparticles can be increased by decreasing the diameter of the particles. This can prove useful for the design of solar energy applications because the band gap can be tuned to most effectively and efficiently capture the solar spectrum. Quantum-confined, wurtzite $CuInS_2$ nanoparticles are also of particular interest, because the wurtzite crystal structure is anisotropic, whereas the chalcopyrite structure is isotropic. This anisotropy will allow the growth of asymmetric nanoparticle morphologies, such as rods or disks. The shape control gives an additional degree of functional tunability. For instance, rods of wurtzite CdS act as light absorbing antennae in photocatalytic systems.[55,56] The anisotropy of the crystal structure is reflected in the directionally dependent effective mass of the hole. Carefully designed structures and systems could take advantage of this to achieve orthogonal charge separation. $CuInS_2$ shares many similarities because it is the ternary derivative of the binary cadmium chalcogenides. It is certainly reasonable to expect similar improvements when shape selectivity is applied to this material.

Furthermore, small $CuInS_2$ nanocrystals are desired because they may demonstrate band gap emission, which was not observed in the larger nano-disks. The larger particles fluoresced at much lower energies than they absorbed, and the cause is thought to be radiative trap states at the

inter-domain grain boundaries present within the larger nanocrystals. If the particles could be prepared with a diameter smaller than the size of those crystal domains, it is expected that the particles would be single-domain and that they would exhibit emission at a wavelength near the band gap. The domain size observed in the large nano-disks is also near to the Bohr exciton radius of wurtzite $CuInS_2$, which is 4.27 nm, according to Dr. Xiao Shen's calculations and Equation 2. A synthesis was thus developed that would produce particles with a diameter smaller than the Bohr exciton radius, which would be quantum-confined.

Experimental

In a typical synthesis of small $CuInS_2$ nanoparticles, $InCl_3$ (111.5 mg, 0.50 mmol), thiourea (77.5 mg, 1.00 mmol), and 5.0 mL of oleylamine were added to a 25.0-mL 3-neck round bottom flask. The reaction mixture was placed under vacuum with stirring at 80 ºC for a minimum of 30 min, at which point the reaction mixture was a clear, colorless mixture with some undissolved solid reactants visible. The flask was then put under N_2 atmosphere, and the temperature was increased to 115 ºC. During the heating process, the solution became pale, clear yellow, with some undissolved reactant still present. A solution of CuOAc (65.0 mg, 0.50 mmol) in diphenyl ether (1.00 mL) and dodecanethiol (DDT, 240 μL, 1.00 mmol) was prepared in a 1-dram vial and was vortexed until cloudy yellow-green. The copper acetate solution was swiftly injected into the hot reaction flask under vigorous stirring. The reaction mixture turned to dark-red and then black within 5 s, and the temperature decreased by ~4 ºC, before recovering to 115 ºC after 2-3 min. The reaction was allowed to proceed for a total of 30 min following the injection. The reaction was stopped by removing the heating mantle and allowing the mixture to

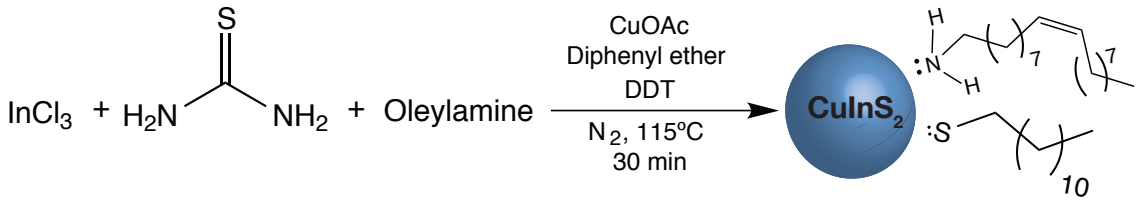

Figure 7. Reaction Scheme for Single-Domain $CuInS_2$ Nanoparticles

cool to below 40 ºC. A portion of unwashed product was diluted in hexanes in a quartz cuvette to collect optical spectra. The remainder of the product was thoroughly washed via precipitation by addition of methanol/ethanol followed by centrifugation for 5 min at 4400 rpm. The clear supernatant was decanted and the precipitate was re-suspended in a solution of DDT in hexanes (1:100 by volume). This washing procedure was repeated at least 3 times. A TEM grid was prepared for the product by diluting the sample in hexanes and drop casting the solution onto a carbon-coated nickel support grid. A general reaction scheme for this procedure can be seen in Figure 7.

Characterization

Transmission Electron Microscopy

Nanoparticle samples produced using this synthesis were analyzed via TEM using both a Philips CM-20 and a Tecnai Osiris Transmission Electron Microscope operating at working voltages of 200 keV. The particles had an average diameter of roughly 2.37 ± 0.31 nm; n = 200 (average diameter ± standard deviation; n = number of particles measured), as can be seen in Figure 8.

The vastly reduced size of these particles compared to the nano-disks is also important because the larger particles possess multiple crystal domains. The average size of those domains,

however, is ~11 nm. This suggests that these smaller particles are likely single-domain in nature. This characteristic of the particles produced in this synthesis is noteworthy because the lack of band gap emission in the larger nano-disks is hypothesized to be caused by the presence of domain boundaries within the crystal.

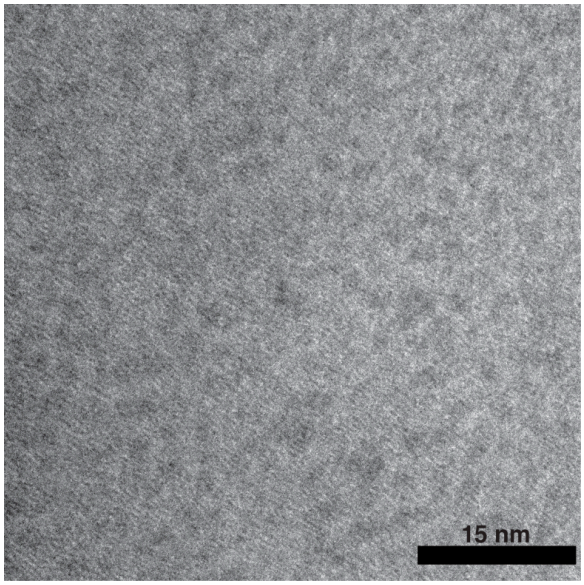

Figure 8. TEM Image of Single-Domain $CuInS_2$ Nanoparticles

Absorbance and Fluorescence Spectra

The absorbance and fluorescence spectra of the product of this synthesis were collected from a dilute solution of particles in hexanes in a quartz cuvette (Figure 9). A JASCO V-670 Spectrophotometer was used to measure the absorbance spectra, and a JASCO FP-8300 Spectrofluorometer was used to record the fluorescence spectra with an excitation wavelength of 348 nm. The absorbance spectrum shows an absorption onset at approximately 600 nm, which is a much shorter wavelength than the ~810 nm onset seen for the larger nano-disks. This indicates that the band gap of these smaller particles is wider than the band gap of the nano-disks, and is

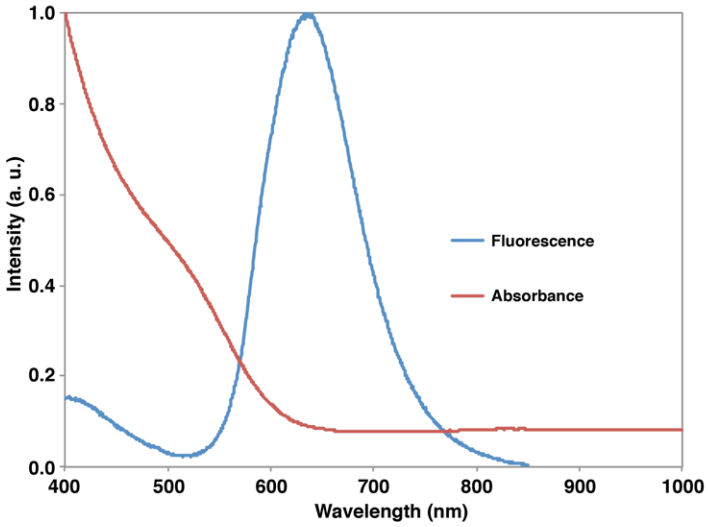

Figure 9. Representative Absorbance and Fluorescence Spectra of Single-Domain $CuInS_2$ Nanoparticles

an effect of the quantum-confinement of the semiconductor nanoparticles. The relatively small Stokes shift of the fluorescence spectrum of the small particles compared to the nano-disks reveals what appears, at first glance, to be band gap emission, and certainly a different radiative pathway than that which was observed for the nano-disks.

Quantum Yield Measurement

The goal of a quantum yield analysis is to determine the amount of photons that are emitted by a sample relative to the amount of photons absorbed. In order to obtain the quantum yield of the particles, a solution of the particles suspended in hexanes was diluted to an optical density of 0.1 at wavelength of 348 nm. A fluorescence spectrum of the same dilute sample of was then collected, with an excitation wavelength of 348 nm. The area under the fluorescence peak was determined, and then this value, along with the absorbance intensity, was compared to those of a fluorophore. The fluorophore used in this study was a solution of Rhodamine B dye in

methanol, which has a known quantum yield of 70% at 348 nm excitation. Equation 3 shows the calculation performed in order to measure the quantum yield of a sample.[73] In the equation,

$$\Phi_f^s = \frac{F^s f_i n_s^2}{F^i f_s n_i^2} \Phi_f^i \quad (3)$$

F^i and F^s represent the emission peak areas for the standard and sample, respectively; f_i and f_s are the absorbance of the standard and the sample, respectively; n_i and n_s represent the refractive indices of the standard and the sample solutions, respectively; Φ^i_f and Φ^s_f are the quantum yields of the standard and sample, respectively.[74]

A high quantum yield percentage would suggest that the material is highly efficient in converting the energy from photons absorbed into photons emitted. The $CuInS_2$ nanoparticles produced by this synthesis typically showed quantum yields in the range of 0.4% to 0.8%. This low quantum yield suggests that much of energy absorbed by the crystals is being released via non-radiative pathways, such as phonon vibrations. It is not unusual for $CuInS_2$ nanoparticles to possess low quantum yields.[52] Reports in the literature for chalcopyrite $CuInS_2$ nanoparticles show quantum yields closer to 4%[75], and typically that value can be improved by ZnS shelling procedures[76,77,78,79,80] to values as high as 70%.[53] The efficiencies for these wurtzite particles are low, but it is reasonable to assume that a shelling procedure may provide improvements.

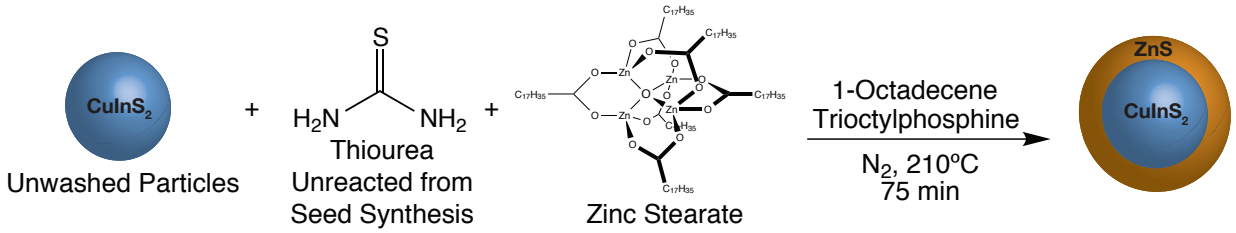

Figure 10. ZnS Shelling Procedure

ZnS Shelling

The quantum yield of the particles was improved by a ZnS shelling procedure which was adapted from a literature procedure for capping chalcopyrite $CuInS_2$ nanocrystals.[53] The modified reaction scheme is shown in Figure 10. In this one-pot procedure, wurtzite $CuInS_2$ nanoparticles were synthesized as previously detailed, but the product was left in the reaction flask at 120 ºC under inert atmosphere before cleaning. A suspension of zinc stearate (253 mg, 0.4 mmol) in 1-octadecene (5.0 mL, 15.6 mmol) and trioctylphosphine (0.5 mL, 1.12 mmol) was prepared and placed under nitrogen. The mixture was vortexed, and a cloudy, milky white solution resulted. The zinc solution was then added drop-wise to the 120 ºC reaction mixture over 6 minutes. The temperature was then increased to 210 ºC, and the reaction mixture was stirred for 75 min at 210 ºC. The solution was a dark-red/black color as in the original particle synthesis. The product of the shelling procedure was precipitated by addition of a 3:1 mixture of methanol and ethanol followed by centrifugation, and the particles were redispersed initially in a mixture of oleylamine:hexanes (1:100 by volume). After the final cycle of washing, the particles were suspended in toluene.

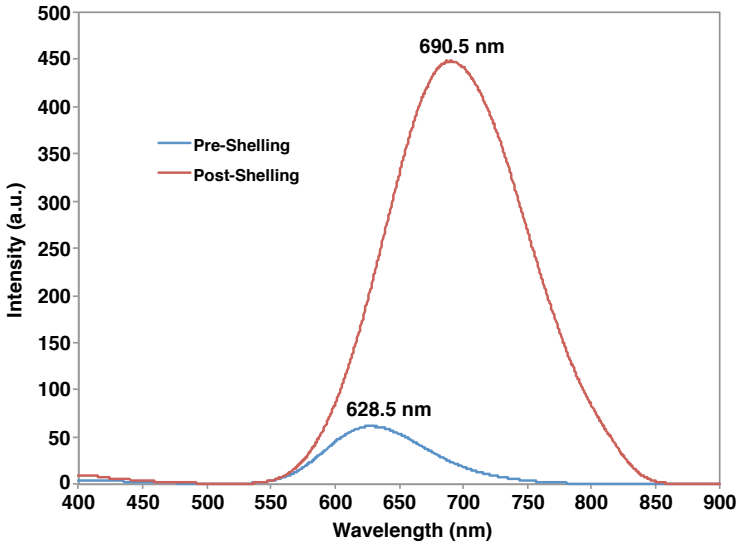

Figure 11. Un-normalized Fluorescence Spectra Before and After ZnS Shelling

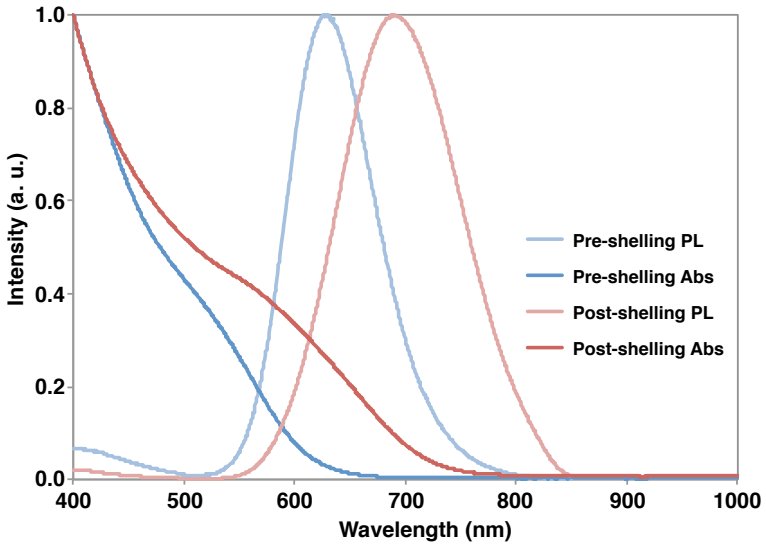

Figure 12. Absorbance and Photoluminescence Spectra Before and After ZnS Shelling

Absorbance and fluorescence spectra were collected on the ZnS-shelled particles, and the quantum yield was calculated. In Figure 11, the raw fluorescence spectra of the unshelled and shelled particles are shown. The quantum yield before shelling was measured to be 0.52%, and after shelling the quantum yield was increased to 7.5%. This represents a nearly 14-fold increase in the quantum yield. This is a great improvement, but it still falls short of the quantum yields that have been achieved with chalcopyrite $CuInS_2$.

A red-shift was observed in the electronic properties of the nanoparticles, which can be seen well in the normalized spectra shown in Figure 12. Following ZnS shelling, a red-shift of similar magnitude (~62 nm) was observed in both the absorbance and fluorescence spectra of the particles. This is an interesting result, because a blue-shift has been typically observed in the literature for shelling of chalcopyrite $CuInS_2$, and it results from the alloying on the surface between the core material and the ZnS.[78] In this process, the alloy formed has a new band gap energy representative of the ratio of the component materials. ZnS has a wider band gap than $CuInS_2$, so an alloy material between the two will have a wider band gap than just $CuInS_2$, therefore a blue-shift in optical spectra would be anticipated.[53]

It must thus be noted that the red-shift observed in the optical spectra after shelling could possibly result from further growth of the particles. The shelling procedure is performed on unwashed particles still in the original reaction medium with any unreacted precursors still present. Additionally, the shelling procedure requires significantly increased temperatures for a long period of time. This could encourage continued particle growth through the addition of unreacted monomers or through ripening processes. TEM images following shelling would be very useful for comparing initial and final particle diameters, but no such images were collected for these early shelling attempts. However, previously, when the particle synthesis was

performed at higher temperatures or for longer times, dramatic changes were not observed in either the positions of the optical spectra or the quantum yields. Further analysis and characterization surrounding the ZnS shelling procedure will be a future direction for this study, namely TEM imaging and Energy Dispersive X-Ray Spectroscopy (EDS).

Powder X-Ray Diffraction

X-Ray Diffraction (XRD) patterns were collected for these small, single-domain $CuInS_2$ nanoparticles using a Scintag XGEN-4000 powder X-ray diffractometer using a Cu K_α X-Ray source ($\lambda = 1.541$ Å). It was hypothesized that these smaller particles would similarly be wurtzite in nature, as it is well known that chalcopyrite is the thermodynamically favored crystal structure and wurtzite is the kinetic product. This synthesis is performed at significantly lower

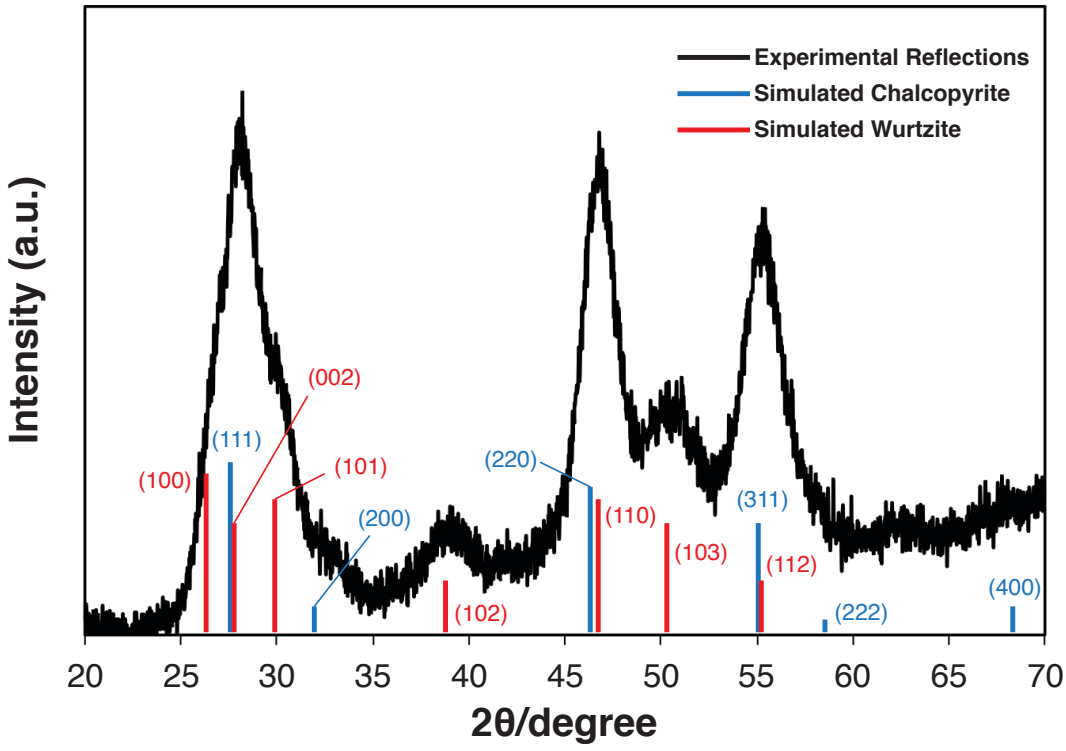

Figure 13. Powder XRD Pattern of Single-Domain $CuInS_2$ Nanoparticles with Characteristic Reflections of Chalcopyrite and Wurtzite Structures

temperatures than required in a typical solution-based synthesis of chalcopyrite $CuInS_2$ nanoparticles, which can be as high as 240-350ºC.[18,81] This lead to the hypothesis that at lower temperatures, the kinetically favored state (wurtzite) could be the predominating product.

Collecting a well-defined and well-resolved reflection pattern for these particles proved to be challenging because of their extremely small size. Scherrer line broadening causes small crystallites to have broader and less intense reflections. This results from there being fewer atomic planes present in smaller crystallites to provide enforcement of the Bragg condition, $n\lambda = 2d\sin\theta$. This broadening effect rendered Selective Area Electron Diffraction (SAED), which can be performed concomitantly with TEM imaging, largely useless for these small particles as the rings broadened to the point of being indistinguishable from one another. Powder XRD analysis suffered from similar problems. The best resolved XRD pattern for a sample of the small $CuInS_2$ nanoparticles is shown in Figure 13.

In the XRD pattern shown, reflection assignments can be made in agreement with the pattern expected for wurtzite $CuInS_2$, which are consistent with those seen in the XRD pattern of the larger nano-disks. In particular, there are reflections located at 39.0º and 50.5º, which are unique and indicative of the wurtzite crystal structure. These reflections result from the (102) and (103) planes of the wurtzite structure, respectively. There are, notably, no overlapping reflections at these angles that could be attributed to the chalcopyrite structure. There is evident broadening of the peaks, as is expected for nanocrystals of decreased diameter. Using the Scherrer Equation

$$D = \frac{0.89\,\lambda}{\beta \cos\theta} \tag{4}$$

(Equation 4), the average crystallite size, *D*, can be estimated for the sample based on the full width at half maximum (FWHM) in radians, β, of the reflections in the XRD pattern. Along with

the wavelength of the X-ray, λ, and the Bragg angle, θ, for the reflection, the average crystallite size for the sample can be determined.[82,83]

Before this analysis can be performed, the FWHMs of the reflections for the sample of interest need to be corrected based on the instrumental line broadening. An XRD pattern was collected on a LaB_6 standard crystalline powder. Because of the highly crystalline nature of the sample, the narrow reflections only show broadening from the instrument itself. The FWHM of a reflection at $2\theta = 30.4^{\circ}$ was measured to be 0.156°. This value was subtracted from the measured FWHM values for the $CuInS_2$ samples.

This analysis was performed on the XRD patterns of both the nano-disks (Figure 5.b) and the smaller nanoparticles (Figure 13). The crystallite size calculated from Equation 4 did show the crystallites to be larger in the nano-disks sample. Scherrer line broadening analysis for the nano-disks was performed using the corrected FWHMs for the reflections at $2\theta = 46.5^{\circ}$ and $2\theta = 55.0^{\circ}$. These reflections were selected for the analysis because they are clearly defined in the XRD patterns of both samples; they represent the (110) and (112) planes of the wurtzite structure. Using these FWHMs and the Cu K_{α} X-Ray wavelength ($\lambda = 0.1541$ nm), the average crystallite size was calculated to be 14.3 nm and 13.6 nm, respectively. These values are smaller than the diameter of the nano-disks as seen in TEM image shown in Figure 5. This was initially thought to be indicative of the fact that these particles are poly-domained, but recent work has suggested otherwise. The underlying sulfur lattice in these particles is uninterrupted even through the domain boundaries, so these larger disks appear single-domain in XRD.[54] The lower calculated crystallite sizes are lower than the diameters seen the TEM image, because the diameters can vary from sample to sample, and the TEM image and XRD pattern in Figure 5 are from two different samples.

Scherrer line broadening analysis was also performed on the smaller single-domain particles using the reflections at those same angles. The crystallite size was calculated to be 4.53 nm and 4.17 nm, respectively. These values are significantly smaller than the crystallite sizes measured for the nano-disks. The average crystallite domain size is quite similar to the typical particle diameters seen in TEM. The slight discrepancy is likely just a result of the particles being very small and difficult to image clearly. Nonetheless, the particles seen in the TEM image (Figure 8) are undeniably smaller than the average crystallite domain size calculated for the nano-disks, and this supports the hypothesis that the smaller particles may be single-domain in nature. This hypothesis is further supported by the fact that the average crystallite size calculated from Scherrer line broadening for the small particles is similar to the measured diameter from TEM. If there were twinning present in the smaller particles, then their average crystallite size would be calculated to be smaller than the particle diameters. This is not the case here, so it is reasonable to determine that the small particles are each a single crystalline domain.

Further powder XRD studies on these single-domain particles have shown difficulties in providing irrefutable evidence of the presence of exclusively wurtzite crystal structure. Conversely, the hypothesis is shifting toward the possibility of the presence of both chalcopyrite and wurtzite $CuInS_2$ because recent XRD patterns do not definitively show only one structure. Indeed, evidence of the presence of both crystal structures can even be seen in the powder XRD pattern shown in Figure 13. The characteristic reflections of both crystal structures are shown beneath the experimental pattern in Figure 13.[18,72] While there are reflections that can be confidently attributed to the wurtzite structure, such as the (102) and (103) planes, the intensities of the reflections do not match the calculated pattern, and this is an indication of the presence of the chalcopyrite structure. In particular, the reflections at 46.5º and 55.0º are much stronger than

expected when compared to the (103) reflection at 50.5º. The intensities of the wurtzite (110) and (112) reflections are augmented by the chalcopyrite (220) and (112) reflections, which are located at nearly the same angles, 46.5º and 55.0º, respectively.

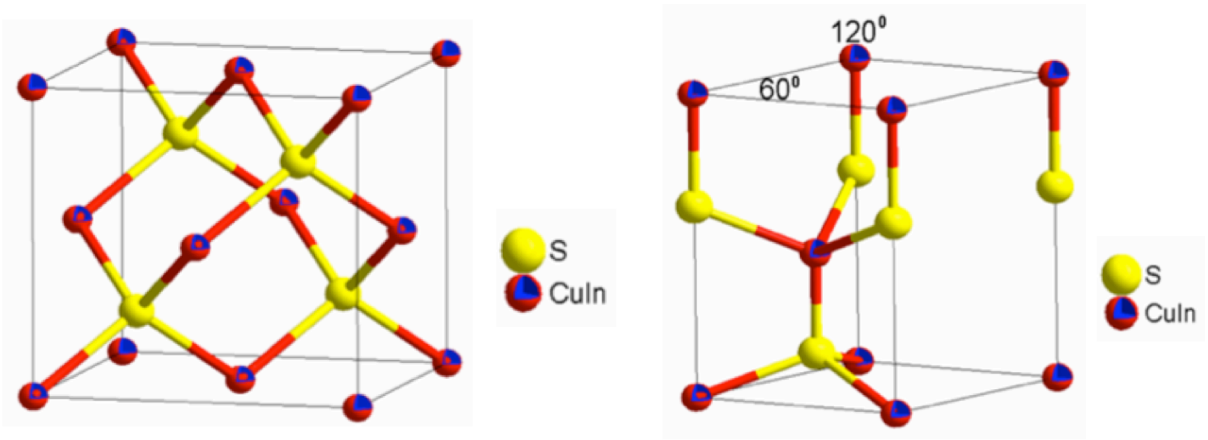

Figure 14. Chalcopyrite (left) and Wurtzite (right) Crystal Structures of $CuInS_2$

There is certainly the presence of both crystal structures in the small $CuInS_2$ nanoparticles, and initially it was unclear if each individual nanocrystal in the sample is of a single crystal structure, either chalcopyrite or wurtzite, or if there is twinning between the two phases in an individual particle. However, the Scherrer line broadening analysis detailed above served to confirm that the small $CuInS_2$ nanoparticles are indeed single-domain and that there is no evidence of twinning in the small particles. Therefore, in any particular sample of small particles produced according to this synthesis, a mixture of individual wurtzite and chalcopyrite particles exist. The chalcopyrite and wurtzite crystal structures can be seen in Figure 14.[72] This is a point of interest for the future directions of this project because it could have a number of implications for the applications of these particles. Each crystal structure can result in unique particle morphologies, and the opto-electronic properties are slightly different. Additionally, it

raises a number of compelling questions about precisely which synthetic conditions in this procedure are responsible for favoring one crystal structure as opposed to the other.

Conclusion

A synthesis was developed that produced small wurtzite $CuInS_2$ nanoparticles. This aim was pursued because it was hypothesized to produce single-domain particles that would exhibit band gap emission, quantum-confinement, and band gap tunability. The synthesis detailed here also produced wurtzite $CuInS_2$ nanoparticles that emit at wavelengths near to their band gap absorption energy. Band gap emission from wurtzite $CuInS_2$ nanoparticles has not yet been reported, and they hold possible future applications for photocatalytic reduction of water. The wurtzite crystal structure of these small particles allows for the possibility that asymmetric morphologies, such as rods or disks, could be grown from these seeds.

The particles produced from this synthesis have diameters according to TEM images near 3.0 nm, which is small enough to be quantum-confined, and they fluoresce at energies very near to their absorbance, which suggested band gap emission. Preliminary efforts to form a ZnS shell improved the quantum yield of the particles to 7.5%. A most interesting observation about this synthesis, though, was the apparent presence of both wurtzite and chalcopyrite structures. The synthetic causes for the formation of both structures are not yet understood, but the future work in this study will focus on preferentially forming only wurtzite particles.

CHAPTER IV

UNIQUE AND UNPREDICTABLE CHARACTERISTICS OF SINGLE-DOMAIN WURTZITE $CuInS_2$ NANOPARTICLES

Introduction

The synthesis detailed throughout the previous chapter produced what were initially thought to be simply quantum-confined, wurtzite $CuInS_2$ nanoparticles that exhibited band gap emission. Further study and analysis outlined in this chapter of these particles has proven that this synthesis and the resultant particles are both significantly more complex and less predictable than initially imagined. Understanding the intricacies surrounding the physical, structural, and energetic characteristics of these particles has been and will continue to be a major goal of this project.

Since band gap tunability was the primary goal, we strove to take advantage of the small size and subsequent quantum confinement effects that could be seen with these smaller particles.[84] The motivation for wanting to manipulate the band gap of the particles arose primarily from their potential future use in Quantum Dot Sensitized Solar Cells (QDSSCs) and other photovoltaic devices.[39] The band gap of a quantum dot determines what wavelengths of light it will be capable of absorbing. This is of great importance in the design of photovoltaic devices because certain energies are required for particular electrochemical reactions. The ability to fine-tune the band gap of these wurtzite $CuInS_2$ nanoparticles would ideally allow for the particles to be used in myriad photovoltaic applications regardless of the energetic requirement. The scope of applicability of this material would be greatly expanded simply by developing a

robust and reliable method to manipulate the band gap of the particles. Strong control over the band gap of the particles created in this synthesis is also desirable because it would prove the reproducibility of reaction. For the material to be of use in photovoltaic devices, there must be a certain amount of confidence that by following an particular procedure, identical particles are produced each time that have highly consistent energetic properties.

Initial efforts to controllably alter the band gap of the single-domain, wurtzite $CuInS_2$ nanoparticles involved manipulating the experimental details of the synthesis described in Chapter III, in an effort to grow smaller or larger nanoparticles. The size of the nanoparticles produced from a typical solution-based synthesis can often be changed by altering simple experimental conditions, such as precursor concentrations[85], precursor reactivity[86], reaction length[87], or reaction temperature[88].

In this synthesis, it was anticipated that the size of the resultant particles could be increased by increasing the reaction time, as the particle growth could continue following the initial nucleation events. Therefore, the reaction time was increased to as long as 3 h. It was also hypothesized that increasing the reactant concentrations would increase particle size because there would be more precursor material to grow from each nucleation event. Reactant concentrations were increased to as high as five times the original procedure. Additionally, it was hypothesized that higher reaction temperatures would produce larger particles as the growth rates would be increased. Thus, the reaction was performed at temperatures ranging from 115 ºC to 200 ºC. Changing these reaction variables proved to have no effect on the band gap of the particles. Additionally, altering the reaction temperature could favor either the wurtzite or chalcopyrite structure due to relative thermodynamic stabilities.

More exotic methods for size control were then attempted, including a seeded growth mechanism. Seed particles were synthesized according to the typical synthesis, after which additional precursor reagents were injected into the reaction mixture. This second wave of injected reagents was expected to grow onto the previously formed nucleation points, and this would increase the overall particle size. This did not prove successful, as additional nucleation events occurred and overall the particles did not increase in size. Attempts were also made using a method called successive ionic layer adsorption and reaction[89], wherein individual monomer layers of sulfur and copper/indium were to be deposited sequentially. This method also did not produce controllable changes in the band gap. Further attempts were then made where the reactivity of the sulfur precursor was altered. A series of different substituted thioureas, such as methylthiourea and acetylthiourea, were incorporated into the reaction, but there was no effect. This result was later found to be consistent with literature on the use of substituted thioureas. According to the reports, the reactivity between metal ions and various substituted thioureas was found to be insignificantly different from the unsubstituted molecule towards metal ions. There exist some differences in solubility in the organic solvent, but the reactivity was not found to differ in any appreciable way under these synthetic conditions.[90]

The next approach that was attempted was to add oleic acid to the initial reaction mixture in discrete molar quantity ratios compared to the metal precursors. The hypothesis that motivated this approach was that the reactivity of the hard In^{3+} ions would be moderated by the binding of the hard carboxylate head groups of the oleic acid. The interaction between the two should be strong according to Hard-Soft Acid Base theory[91], and their association would moderate their participation in nucleation events once the copper precursor was injected. Fewer nucleation events would mean that there were fewer growing particles onto which the precursor materials

could deposit, so the particles that did form would grow to be larger than the particles formed with no oleic acid present.[52]

Initial attempts following this method showed promising results, where the absorbance curve of the particles shifted toward longer wavelengths of light, indicating that the band gap of the particles had been narrowed. Several syntheses were performed with different amounts of oleic acid, and it appeared that increased oleic acid concentrations resulted in a successively more narrow band gap (red-shift), as can be seen in Figure 15. This observation was in

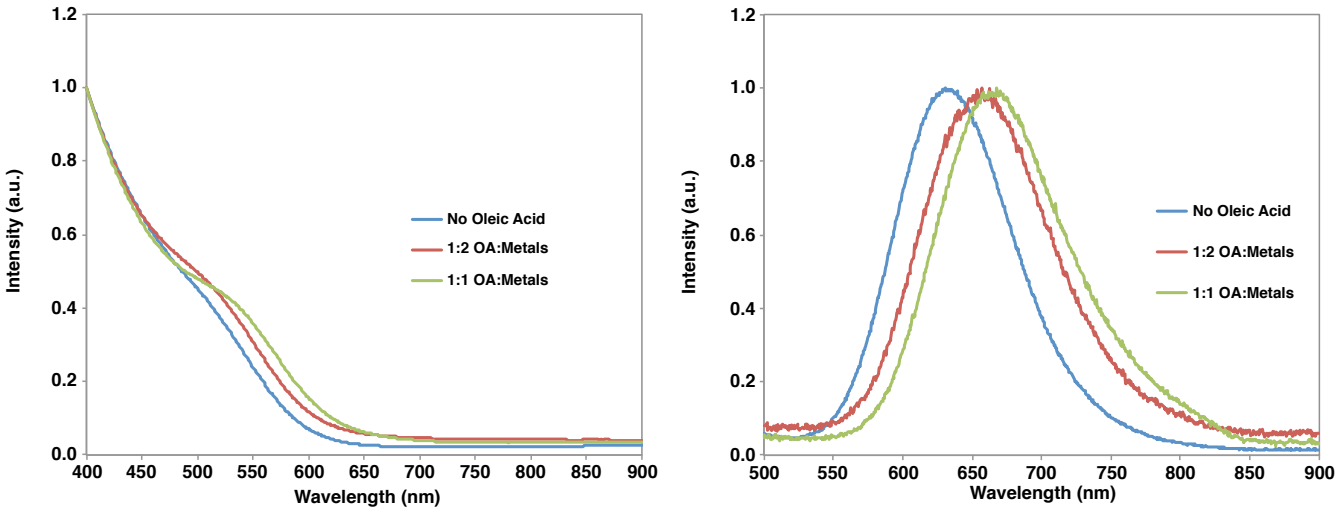

Figure 15. Absorbance and Fluorescence Spectra Showing Red-Shift with Increased Oleic Acid Concentrations

agreement with the initial hypothesis, and it encouraged further investigation into the synthesis as a whole and further characterization of the particles to determine if the trends were reproducible and understandable.

The red-shift observed in the spectra suggested that the diameter of the particles was increasing with increased concentrations of oleic acid. TEM images of these early samples seemed to support this hypothesis as well, with an increase in the average diameter by

approximately 1.00 nm from performing the reaction with no oleic acid compared to having a 1:1 ratio of oleic acid to metal precursors.

A second hypothesis that needed to be investigated was the possibility that the composition of the particles was being altered, namely the [Cu]:[In] ratio. If the presence of oleic acid was preventing some of the indium from reacting, then it would be expected that the resultant particles would be copper-rich. A change in stoichiometric ratio of a semiconductor material can have a very strong effect on its band gap. It has been observed in chalcopyrite $CuInS_2$, that copper-rich nanoparticles show a narrowed band gap, whereas copper-poor particles show a widened band gap.[52] If a similar behavior occurs for wurtzite $CuInS_2$ nanoparticles, then an increase in oleic acid concentration should produce Cu-rich particles with narrower band gaps, which is the very trend observed in the initial results..

However, which of these possible changes in the particles produced in the presence of oleic acid was most responsible for the apparent changes in the band gap of the particles? Could each factor be contributing simultaneously? These questions needed to be fully explained, and it also needed to be determined whether the initial results represented a reproducible trend.

Experimental Description

Synthetic Description

A schematic of this reaction is represented in Figure 16. The synthesis very closely mirrors that which was detailed in Chapter III. The only difference was that during a given reaction, a distinct amount of oleic acid (0.25 mmol, 0.5 mmol, or 1.0 mmol) was included in the reaction flask along with indium (III) chloride, thiourea, and oleylamine. These molar quantities

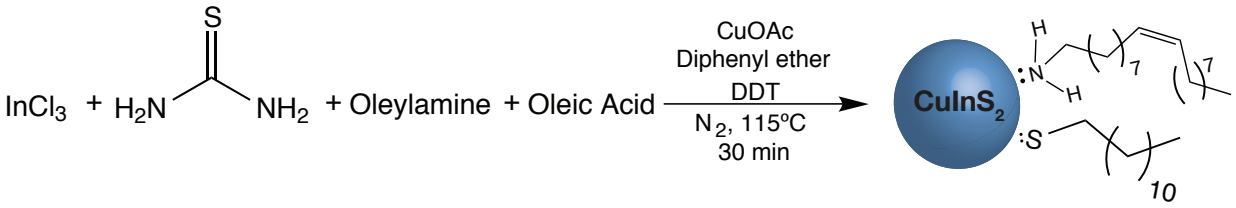

Figure 16. Reaction Scheme of Synthesis with Oleic Acid

of oleic acid corresponded to a 1:2, 1:1, and 2:1 molar ratio of oleic acid to metal precursors (copper and indium). Optical spectra were collected on a dilute solution of the particles suspended in neat hexanes. All TEM images were collected by diluting the particles in neat hexanes and drop casting the solution onto a carbon-coated nickel support grid. Further characterization and analysis was performed on the particles, including quantum yield measurements, Inductively Coupled Plasma-Optical Emission Spectroscopy (ICP-OES), and powder XRD. Additionally, quantum-confinement calculations were performed for these particles to elucidate some of the energetic properties of these samples.

TEM Images and Particle Sizing

Nanoparticle samples produced using this synthesis were analyzed via TEM using both a Philips CM-20 and a Tecnai Osiris Transmission Electron Microscope operating at working voltages of 200 keV. Particles were sized from analysis of TEM images. Average particle sizes were determined by measuring a minimum of 100 particles, with a target of 200. Average particle diameters are reported with corresponding standard deviations.

Apparent Band Gap from Absorbance Onset

The absorbance onset by a quantum dot is indicative of the energy needed to form an exciton pair. Therefore, the onset of peak absorbance can be used to estimate the band gap

$$[\alpha \times h\nu]^2 = \left[\frac{(1-Abs)^2}{2(Abs)} \times h\nu\right]^2 \quad (5)$$

energy for a particular sample of quantum dots. The band gap of a quantum dot sample can be determined from a Tauc plot, where $[\alpha \times h\nu]^2$ is plotted against hν, where α is the absorption coefficient and hν is the energy of the incident photon in eV. This analysis is valid for determining the band gap energy of a direct band gap semiconductor.[92]

The absorption coefficient of wurtzite $CuInS_2$ is not definitively known, so it was necessary to use an approximation of the Tauc relationship. The approximation can be seen in Equation 5, and allows for the apparent band gap energy to be related to the absorbance of the sample at each wavelength of light.[93] This approximation was then plotted against hν on the x-axis, and a line was fitted to the linear portion of the plot. The x-intercept of the line-of-best-fit represents an approximation of the absorbance onset in eV. It is the extrapolated intercept of the

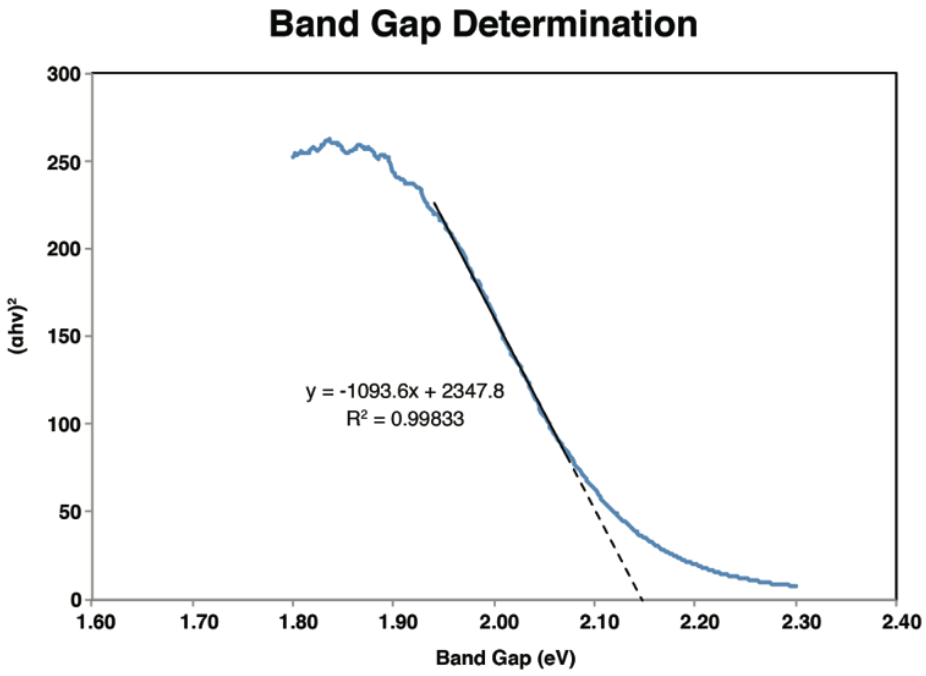

Figure 17. Example of a Plot for Band Gap Determination

linear portion of the resulting curve that approximates the band gap energy. An example of such a plot with its corresponding line-of-best-fit can be seen in Figure 17. In this example, the band gap was found to be 2.15 eV, which is a reasonable value for quantum-confined wurtzite $CuInS_2$. The bulk band gap energy for wurtzite $CuInS_2$ is calculated to be at most 0.08 eV lower than the bulk band gap of chalcopyrite $CuInS_2$, which would give a value of 1.45 eV. These calculated band gap energies will be refered to as apparent band gap energies throughout the rest of this document. All of the apparent band gap energies for various samples will be detailed in the results section of this chapter.

Fluorescence Peak

Fluorescence spectra on the samples produced were collected as outlined in Chapter III, and the measured values were compared to apparent band gap energies, particle compositions, and particle diameters.

ICP-OES and [Cu]:[In] Ratio

The stoichiometry of the samples, namely the [Cu]:[In] molar ratio, was determined by using ICP-OES. The particles were digested in 2% HNO_3, and the analysis was performed using a Perkin Elmer Optima 7000 DV spectrometer. The solution of the digested particles was ignited, and the concentrations of the component elements were determined based on the wavelengths and intensities of emissions from the sample compared to external standards. The concentrations of Cu and In were converted into a molar ratio.

Predicted Band Gap and Diameter from Quantum-Confinement

The particles produced in this synthesis are smaller than the Bohr exciton radius calculated for wurtzite $CuInS_2$. It was reasonable to expect quantum-confinement effects to be seen for these particles. The result of quantum confinement is that the band gap energy of a quantum dot will increase with decreasing particle diameter according to the Brus equation, which was shown previously and is shown again here as Equation 6. Using the effective mass of

$$E_{gap}^{*} = E_{gap}^{bulk} + \frac{h^2}{8r^2}\left[\frac{1}{m_e^* m_o} + \frac{1}{m_h^* m_o}\right] - \frac{1.8e^2}{4\pi\varepsilon\varepsilon_0 r} \quad (6)$$

the hole and electron for wurtzite $CuInS_2$, which are 1.49 m_0 and 0.15 m_0, respectively, the expected band gap energy for a particle of a known radius can be calculated. This predicted band gap energy could then be compared to the apparent band gap energy that was already calculated from the absorbance spectrum.

Additionally, Equation 6 could be rearranged to solve for a radius, *r*, that would correspond to an apparent band gap energy determind from an absorbance spectrum. Each of these analyses required a couple of assumptions: the band gap energy of bulk chalcopyrite $CuInS_2$ was used, as was the dielectric constant of chalcopyrite $CuInS_2$, ε =11.[58] Calculations performed by Dr. Shen have determined the band gap energy of ordered wurtzite phases in $CuInS_2$ to be very close to that of chalcopyrite, and, in disordered wurtzite phases, the band gap is typically 0.3 to 0.5 eV lower than that of chalcopyrite.[59] In the interest of consistency among all quantum-confinement calculations, it was decided to use the band gap energy of bulk chalcopyrite, which is 1.53 eV. The predicted band gap energy and the predicted diameter for a nanoparticle sample was compared to the apparent band gap energy and the measured particle

diameter in order to determine if the change in properties for these particles was dominated by quantum-confinement effects.

Results and Discussion

The synthesis detailed in this chapter was repeated sixteen times with no oleic acid present in the reaction mixture, in order to probe the reproducibility of the properties of the resultant particles. Would the synthesis produce the same apparent band gap consistently? No declaration of trends in data could be made until this was known. The apparent band gaps of these sixteen samples are listed in Table 2, and visualized Figure 18. The range in the apparent band gaps for all data points is 0.32 eV. This disparity between the properties of different

Table 2. Apparent Band Gaps of all Samples Synthesized with no Oleic Acid

Sample Number (No Oleic Acid)	Apparent Band Gap (eV)
i	2.04
ii	2.08
iii	2.07
iv	2.08
v	2.04
vi	1.91
vii	1.88
viii	1.98
ix	1.95
x	1.83
xi	1.96
xii	1.93
xiii	1.98
xiv	1.93
xv	1.90
xvi	2.15
Average Band Gap	1.98
Standard Dev.	0.09

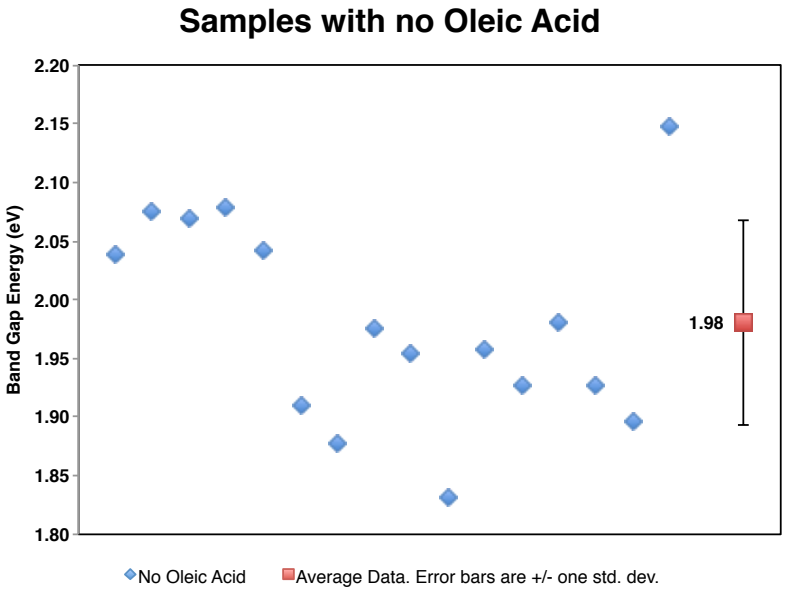

Figure 18. Plot of all Apparent Band Gaps for Samples Synthesized with no Oleic Acid

samples of particles likely results from the inconsistencies associated with this synthesis. Any slight difference in the heating rate and temperature of the reaction mixture could have an effect on the solubility and reactivity of the precursors. Different stirring rates or stirring efficiencies could cause inconsistent dispersion of the precursors throughout the reaction medium resulting in concentration gradients. Inefficient stirring could also result in irreproducible temperatures throughout the reaction mixture. Additionally, the copper source for this reaction is injected in the form of a solution, so the injection rate could affect whether a single nucleation event occurs. Furthermore, the copper source was more of a cloudy dispersion than a clear solution, so it is certainly possible that the reagent is not fully solubilized upon injection, or that the copper may be dissolved to varying degrees. An additional source of variability could be from the rate of cooling to stop the reaction, as the particles may have grown for slightly different amounts of time. This large degree of variability in this synthesis will make it very difficult to definitively prove any trends in the data for particles synthesized with various amounts of oleic acid in the reaction mixture.

ICP-OES was used to measure the [Cu]:[In] ratio for particles synthesized with varying amounts of oleic acid. These [Cu]:[In] molar stoichiometric ratios are of interest because it has been shown that the relative amounts of copper or indium in a sample of chalcopyrite $CuInS_2$ can affect the optical and energetic properties of the particles.[75,94] It is reasonable to assume this could occur with wurtzite $CuInS_2$ as well. The ratios are visualized in Figure 19, where no correlation between copper and indium was apparent relative to the amount of oleic acid present. This indicates that there must be some other kinetic and thermodynamic factors affecting the stoichiometric composition of the particles. Oleic acid does not appear to have a singular dramatic effect on the [Cu]:[In] ratio of the final product.

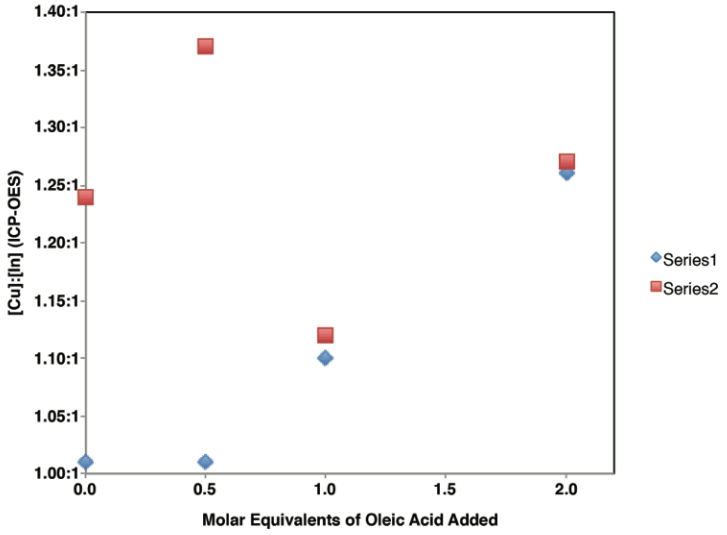

Figure 19. Molar Equivalents of Oleic Acid Versus Particle Stoichiometry

The variability among the identically prepared datasets is not fully understood. The project would benefit from collecting additional data sets. Whether there is or is not a trend between the amount of oleic acid in the reaction and the [Cu]:[In] ratio, richer data may provide a more convincing conclusion.

As previously mentioned, the hypothesis that motivated this portion of the study was that the addition of discrete molar quantities of oleic acid would have an effect on the band gap of the particles and perhaps the diameter as well. Namely, it was hypothesized that increased amounts of oleic acid would lead to larger particles that would be copper-rich with narrower band gaps. In order to analyze whether these or any other trends exist, multiple samples of particles synthesized with four different amounts of oleic acid were fully analyzed, and the data can be seen compiled in Table 3. The table includes the apparent band gap energy, the fluorescence peak wavelength, the measured particle diameter, the predicted band gap energy, the predicted particle diameter, and the particle composition based on ICP-OES. A series of scatterplots is shown in Figure 20, which relate various metrics from Table 3, to identify trends in the data.

Table 3. Data Analyzed for Presence of Trends

Sample Number	Apparent Band Gap (eV)	Fluorescence Peak (eV)	Diameter (TEM)	Predicted Band Gap (eV) (Brus Equation)	Predicted Diameter (nm) (Brus Equation)	[Cu]:[In] (ICP-OES)	Molar equiv. of Oleic Acid
1	2.08	1.96	2.37 ± 0.31 nm; n=200	3.30	4.08		0
2	2.10	1.89	2.88 ± 0.45 nm; n=200	2.70	4.02		0.5
3	2.01	1.86	3.36 ± 0.43 nm; n=200	2.37	4.33		1
4	2.05	1.94	3.73 ± 0.40 nm; n=150	2.20	4.18		2
5	2.04	1.95	2.60 ± 0.24 nm; n=100	2.98	4.21		0
6	2.03	1.93					0.5
7	2.11	1.95	3.12 ± 0.26 nm; n=100	2.51	3.97		1
8	1.96	1.93	2.76 ± 0.20 nm; n=100	2.81	4.56	1.01:1	0
9	1.88	1.93	3.40 ± 0.30 nm; n=100	2.35	4.99	1.01:1	0.5
10	2.00	1.97				1.10:1	1
11	1.83	1.91	3.07 ± 0.29 nm; n=120	2.55	5.36	1.26:1	2
12	2.15	1.95				1.24:1	0
13	1.80	1.90				1.37:1	0.5
14	2.02	1.99				1.12:1	1
15	1.93	1.98				1.27:1	2

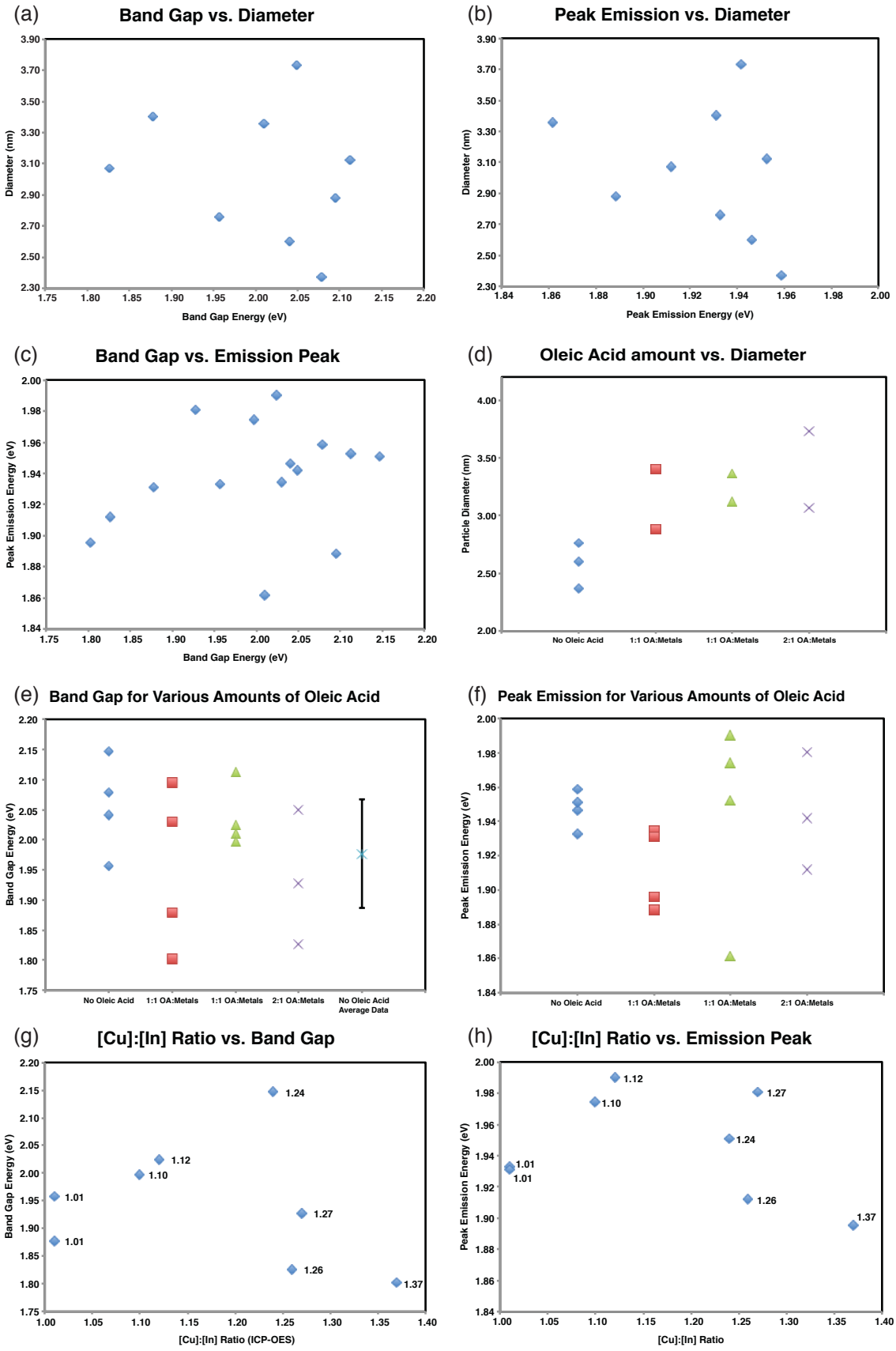

Figure 20. Visualization of data from Table 3

A visual inspection of the eight scatterplots presented in Figure 20 shows that there are no strongly correlating trends among the data. There is perhaps a weak correlation between the amount of oleic acid added to the reaction and the size of the particles produced. It appears that more oleic acid may result in slightly larger particles, but that correlation is not terribly strong. If a correlation is indeed present, then collecting a larger number of data points may allow it to be seen with statistical significance. A statistical Analysis of Variance (ANOVA) test was used to test for any correlation between the data sets for the band gap, emission peak, and particle diameter versus the amount of oleic acid present in the reaction. The results for all three ANOVA tests were negative, indicating that according to the data in Table 3, there is no statistically significant change in calculated band gap energy, peak emission wavelength, or particle diameter based on the amount of oleic acid added to the reaction mixture.

It is also important to note that there is in fact a large amount of variability in the band gap energy of samples of particles prepared with no additional oleic acid. As discussed previously, the apparent band gap energies were calculated for seventeen samples prepared with no oleic acid, and the range in values was found to be 0.32 eV. The variability of the band gaps that resulted from varying the amounts of oleic acid are not much greater than the range of values seen in the multiple iterations of the synthesis performed with no oleic acid present. It is thus very possible that all observed changes in band gap are simply the variable nature of the typical synthesis.

There is also no clear trend between the stoichiometry of the particles and their band gap or fluorescence peaks either, which is interesting because it has been shown in chalcopyrite $CuInS_2$ nanoparticles that copper-rich particles have narrower band gaps, whereas indium-rich

particles have wider band gaps.[52] The data presented here for these wurtzite particles shows no clear correlation.

What is perhaps the most interesting result from this data analysis is the apparent lack of trend between the band gaps and fluorescence peaks of the samples. It was assumed that these single-domain, wurtzite nanoparticles were showing band gap emission because the emission onset and peak were focused so near to the absorption onset. However, if the emission were indeed band gap emission being caused by the recombination of the exciton pair from the conduction band down to the valence band, it would be expected that any change in the band gap would cause a comparable change in the emission peak. The data here shows quite the opposite; there is no correlation between the two metrics. The variation in the band gap energy for the particles sampled in Table 3 is 0.25 eV, but the variation in the emission peaks much more narrow at only 0.13 eV. A Pearson correlation coefficient analysis was performed on the band gap energy relative to the fluorescence peaks, and the coefficient was ~0.25, indicating a very poor level of correlation between the two data sets.

The band gap of the particles is evidently able to vary quite widely, but the fluorescence peak will remain significantly more centered around 1.93 eV. The most likely explanation for this observation is that the fluorescence of the particles synthesized according to this procedure is not band gap emission. Emissive trap state recombination pathways have been observed in chalcopyrite $CuInS_2$ nanoparticles, thus it is not entirely unrealistic that there is a similar mechanism at play here.

Since the emission is situated so close to the band gap energy, if the recombination does involve a trap state, it must be a fairly shallow trap state, so that the emission is not at a drastically reduced energy. Fluorescence of chalcopyrite $CuInS_2$ particles has been attributed to a

donor-acceptor (D-A) transition[75]. It has been established that in the fluorescence of chalcopyrite $CuInS_2$, copper vacancies act as the acceptor state, and sulfur vacancies or copper/indium substitutions act as the donor.[95] It is reasonable to expect the fluorescence of wurtzite $CuInS_2$ to act in a similar manner. Because the D-A pairs are so closely tied to the composition of the particles, it is not at all surprising to see such variability in the opto-electronic properties of the particles produced by this synthesis, given the inconsistency in their stoichiometric compositions. Slight variations in the relative amounts of copper and sulfur could lead to different imperfections in the crystal structure of the particles, causing differences in the energy levels attributed to the D-A transition.

An interesting result of this study was the observed fluorescence coming from $CuInS_2$ nanoparticles that were determined to be copper-rich from ICP-OES analysis. It has been reported in literature that chalcopyrite nanoparticles of $CuInS_2$ with a 1:1:2 composition exhibit no photoluminescence, and noticeable emission is not seen without increasing copper deficiency.[94,53] The synthesis detailed in this study has been shown to produce $CuInS_2$ nanoparticles that are copper-rich to varying degrees, and all of the particles were seen to be weakly, yet noticeably, fluorescent. This result is contrary to previous reports, and merits further investigation.

The single-domain, wurtzite $CuInS_2$ nanoparticles are, as was already established, small enough in diameter to be within the realm of quantum-confinement, as their radius is smaller than the Bohr exciton radius of the material of 4.27 nm. As such, it was expected that slight changes in the particle size would cause a corresponding change in the band gap energy according to the effective masses of the hole and the electron of the particle. It was already

detailed how the Brus equation could be used to predict the band gap based on a measured particle radius or to predict the particle radius based on the apparent band gap energy.

By performing this analysis, these predicted values were calculated for the applicable samples, and the data can be seen in Table 3. The quantum-confinement calculations do not adequately account for the changes seen in the apparent band gap of these particles relative to the bulk chalcopyrite band gap, which is assumed to be similar to that of wurtzite $CuInS_2$. The predicted band gap energy based on the measured particle diameter was consistently larger than the apparent band gap energy determined from the absorbance spectra. Furthermore, the predicted particle radii based on the apparent band gap energies were consistently larger than the particles appeared to be in TEM images. This is evidence of the fact that quantum-confinement effects are not solely responsible for the changes in band gap energy of the particles produced in this synthesis. The optical properties of chalcopyrite $CuInS_2$ is highly dependent of crystal defects, and it appears that these particles may be equally susceptible to intricacies caused by defects.[96,97,98,99]

It was mentioned in Chapter III that XRD analysis has lead to the hypothesis that this synthesis may produce a sample composed of some particles that exhibit the wurtzite structure and some that exhibit the chalcopyrite structure. The inherent variability of the synthesis means that each time a sample is produced, it may have a different ratio of the two crystal structures. This could have important consequences in the opto-electronic properties of the particles. As mentioned previously, our collaborator Dr. Xiao Shen has calculated the band gap of wurtzite $CuInS_2$ to range from being quite similar to that of chalcopyrite to being 0.01-0.08 eV lower in energy, depending on the amount of cation order in the wurtzite phase. It is unknown, but possible, that one of the crystal structure dominates the absorbance of the samples, while the

other crystal structure dominates the emission. Incidentally, the emission observed here is highly reminiscent of that observed for chalcopyrite $CuInS_2$ nanoparticles[52]. This would mean that the relative amounts of wurtzite to chalcopyrite particles in a given sample could vastly change the observed opto-electronic properties because the absorbance and emission energies could each be skewed toward higher or lower energies independent of one another. Furthermore, if the level of cation order in the wurtzite structure has an effect on the band gap energy, then that is an additional factor that could manipulate the apparent band gap of a sample of particles. All of this to say that this is a highly variable synthesis that appears to have many compounding factors that yield the opto-electronic properties and these factors are not yet well understood.

Conclusion

The effort to develop a modified synthesis for single-domain, wurtzite $CuInS_2$ nanoparticles that would allow for limited control over the size and optical properties of the particles has proven to be less straightforward and simple than originally expected. All of the usual techniques to achieve such tunability failed to show any appreciable results, and the method that had initially shown promising results and trends unfortunately turned out to be indistinguishable from the high variability present in the typical procedure from Chapter III. We were unable to pinpoint any solid trends in the data after manipulating the synthesis in various ways. What has instead been gained from this study is a real appreciation for how complicated and unique nanoparticle syntheses can sometimes be.

With each effort toward fine-tuning the synthesis and characterizing the resultant particles, more questions have been raised. The unique and highly unpredictable optical

properties are not yet fully understood, and elucidating the absorption and emission pathways has become a major goal of this research project. It is no longer believed that these wurtzite particles are showing simple band gap absorbance and emission, and this is not an entirely shocking result considering the unique energetic properties observed in chalcopyrite $CuInS_2$. This is only one of the questions that future work on this project will seek to answer. An additional question that has arisen about this project focuses on the crystal structure of the small particles. Initial powder XRD patterns showed clear evidence of the wurtzite crystal structure. More recently collected patterns appear to indicate a mixture of wurtzite and chalcopyrite crystal structures, perhaps representing that from one nanoparticle to the next neither the thermodynamic nor the kinetic structure is entirely favored. This question of which crystal structure is predominantly produced by this reaction is of paramount interest for this project because the development of a reliable synthesis for producing wurtzite, quantum-confined $CuInS_2$ nanocrystals is a major focus.

There remain a large number of unknowns surrounding this new synthesis, and answering those questions will improve the understanding of the material for all researchers interested in it. Once the intricacies of this synthesis have been successfully detailed and understood, the future use of wurtzite $CuInS_2$ nanoparticles toward the photocatalytic reduction of water, in quantum dot sensitized solar cells, or in other photovoltaic devices may be possible.

REFERENCES

1. Schaak, R. E.; Williams, M. E., Full Disclosure: The Practical Side of Nanoscale Total Synthesis. *ACS Nano* **2012,** *6* (10), 8492-8497.

2. Hughes, B. K.; Luther, J. M.; Beard, M. C., The Subtle Chemistry of Colloidal, Quantum-Confined Semiconductor Nanostructures. *ACS Nano* **2012,** *6* (6), 4573-4579.

3. Skrabalak, S. E.; Xia, Y., Pushing Nanocrystal Synthesis toward Nanomanufacturing. *ACS Nano* **2009,** *3* (1), 10-15.

4. Bouzigues, C.; Gacoin, T.; Alexandrou, A., Biological Applications of Rare-Earth Based Nanoparticles. *ACS Nano* **2011,** *5* (11), 8488-8505.

5. Barry, N. P. E.; Sadler, P. J., Challenges for Metals in Medicine: How Nanotechnology May Help To Shape the Future. *ACS Nano* **2013,** *7* (7), 5654-5659.

6. Atsushi, O.; Tagoh, H.; Lee, T.; Kuritani, T.; Takahara, Y.; Shimamura, T.; Ikegami, H.; Kurimoto, M.; Yoshizaki, K.; Kishimoto, T., A new highly sensitive immunoassay for cytokines by dissociation-enhanced lanthanide fluoroimmunoassay (DELFIA). *Journal of Immunological Methods* **1992,** *148* (1–2), 15-22.

7. Park, K., Facing the Truth about Nanotechnology in Drug Delivery. *ACS Nano* **2013,** *7* (9), 7442-7447.

8. Serpone, N.; Emeline, A. V., Semiconductor Photocatalysis — Past, Present, and Future Outlook. *The Journal of Physical Chemistry Letters* **2012,** *3* (5), 673-677.

9. Lohse, S. E.; Murphy, C. J., Applications of Colloidal Inorganic Nanoparticles: From Medicine to Energy. *Journal of the American Chemical Society* **2012,** *134* (38), 15607-15620.

10. Kramer, I. J.; Sargent, E. H., Colloidal Quantum Dot Photovoltaics: A Path Forward. *ACS Nano* **2011,** *5* (11), 8506-8514.

11. Lewis, N. S.; Nocera, D. G., Powering the planet: Chemical challenges in solar energy utilization. *Proceedings of the National Academy of Sciences* **2006,** *103* (43), 15729-15735.

12. Kamat, P. V., Meeting the Clean Energy Demand: Nanostructure Architectures for Solar Energy Conversion. *The Journal of Physical Chemistry C* **2007,** *111* (7), 2834-2860.

13. Walter, P.; Welcomme, E.; Hallégot, P.; Zaluzec, N. J.; Deeb, C.; Castaing, J.; Veyssière, P.; Bréniaux, R.; Lévêque, J.-L.; Tsoucaris, G., Early Use of PbS Nanotechnology for an Ancient Hair Dyeing Formula. *Nano Letters* **2006,** *6* (10), 2215-2219.

14. Pérez-Arantegui, J.; Molera, J.; Larrea, A.; Pradell, T.; Vendrell-Saz, M.; Borgia, I.; Brunetti, B. G.; Cariati, F.; Fermo, P.; Mellini, M.; Sgamellotti, A.; Viti, C., Luster Pottery from the Thirteenth Century to the Sixteenth Century: A Nanostructured Thin Metallic Film. *Journal of the American Ceramic Society* **2001,** *84* (2), 442-46.

15. Padovani, S.; Sada, C.; Mazzoldi, P.; Brunetti, B.; Borgia, I.; Sgamellotti, A.; Giulivi, A.; D'Acapito, F.; Battaglin, G., Copper in glazes of Renaissance luster pottery: Nanoparticles, ions, and local environment. *Journal of Applied Physics* **2003,** *93* (12), 10058-10063.

16. Yuan, W.; Jiang, G.; Che, J.; Qi, X.; Xu, R.; Chang, M. W.; Chen, Y.; Lim, S. Y.; Dai, J.; Chan-Park, M. B., Deposition of Silver Nanoparticles on Multiwalled Carbon Nanotubes Grafted with Hyperbranched Poly(amidoamine) and Their Antimicrobial Effects. *The Journal of Physical Chemistry C* **2008,** *112* (48), 18754-18759.

17. Guzman, J.; Gates, B. C., Catalysis by Supported Gold: Correlation between Catalytic Activity for CO Oxidation and Oxidation States of Gold. *Journal of the American Chemical Society* **2004,** *126* (9), 2672-2673.

18. Nose, K.; Soma, Y.; Omata, T.; Otsuka-Yao-Matsuo, S., Synthesis of Ternary $CuInS_2$ Nanocrystals; Phase Determination by Complex Ligand Species. *Chemistry of Materials* **2009,** *21* (13), 2607-2613.

19. Brus, L. E., Electron–electron and electron‐hole interactions in small semiconductor crystallites: The size dependence of the lowest excited electronic state. *The Journal of Chemical Physics* **1984,** *80* (9), 4403-4409.

20. Zheng, L.; Xu, Y.; Song, Y.; Wu, C.; Zhang, M.; Xie, Y., Nearly Monodisperse $CuInS_2$ Hierarchical Microarchitectures for Photocatalytic H_2 Evolution under Visible Light. *Inorganic Chemistry* **2009,** *48* (9), 4003-4009.

21. Han, Z.; Qiu, F.; Eisenberg, R.; Holland, P. L.; Krauss, T. D., Robust Photogeneration of H_2 in Water Using Semiconductor Nanocrystals and a Nickel Catalyst. *Science* **2012,** *338* (6112), 1321-1324.

22. Kudo, A.; Sekizawa, M., Photocatalytic H_2 evolution under visible light irradiation on Ni-doped ZnS photocatalyst. *Chemical Communications* **2000,** (15), 1371-1372.

23. Costi, R.; Saunders, A. E.; Elmalem, E.; Salant, A.; Banin, U., Visible Light-Induced Charge Retention and Photocatalysis with Hybrid CdSe−Au Nanodumbbells. *Nano Letters* **2008,** *8* (2), 637-641.

24. Elmalem, E.; Saunders, A. E.; Costi, R.; Salant, A.; Banin, U., Growth of Photocatalytic CdSe–Pt Nanorods and Nanonets. *Advanced Materials* **2008,** *20* (22), 4312-4317.

25. Tsuji, I.; Kato, H.; Kobayashi, H.; Kudo, A., Photocatalytic H_2 Evolution Reaction from Aqueous Solutions over Band Structure-Controlled $(AgIn)_xZn_{2(1-x)}S_2$ Solid Solution Photocatalysts with Visible-Light Response and Their Surface Nanostructures. *Journal of the American Chemical Society* **2004,** *126* (41), 13406-13413.

26. Tsuji, I.; Kato, H.; Kobayashi, H.; Kudo, A., Photocatalytic H_2 Evolution under Visible-Light Irradiation over Band-Structure-Controlled $(CuIn)_xZn_{2(1-x)}S_2$ Solid Solutions. *The Journal of Physical Chemistry B* **2005,** *109* (15), 7323-7329.

27. Klenk, R.; Klaer, J.; Scheer, R.; Lux-Steiner, M. C.; Luck, I.; Meyer, N.; Rühle, U., Solar cells based on $CuInS_2$—an overview. *Thin Solid Films* **2005,** *480–481* (0), 509-514.

28. Smith, A. M.; Nie, S., Semiconductor Nanocrystals: Structure, Properties, and Band Gap Engineering. *Accounts of Chemical Research* **2009,** *43* (2), 190-200.

29. Wood, A.; Giersig, M.; Mulvaney, P., Fermi Level Equilibration in Quantum Dot−Metal Nanojunctions. *The Journal of Physical Chemistry B* **2001,** *105* (37), 8810-8815.

30. Gur, I.; Fromer, N. A.; Geier, M. L.; Alivisatos, A. P., Air-Stable All-Inorganic Nanocrystal Solar Cells Processed from Solution. *Science* **2005,** *310* (5747), 462-465.

31. Kamat, P. V.; Tvrdy, K.; Baker, D. R.; Radich, J. G., Beyond Photovoltaics: Semiconductor Nanoarchitectures for Liquid-Junction Solar Cells. *Chemical Reviews* **2010,** *110* (11), 6664-6688.

32. Teoh, W. Y.; Scott, J. A.; Amal, R., Progress in Heterogeneous Photocatalysis: From Classical Radical Chemistry to Engineering Nanomaterials and Solar Reactors. *The Journal of Physical Chemistry Letters* **2012,** *3* (5), 629-639.

33. Shen, S.; Wang, Q., Rational Tuning the Optical Properties of Metal Sulfide Nanocrystals and Their Applications. *Chemistry of Materials* **2012,** *25* (8), 1166-1178.

34. Hoffmann, M. R.; Martin, S. T.; Choi, W.; Bahnemann, D. W., Environmental Applications of Semiconductor Photocatalysis. *Chemical Reviews* **1995,** *95* (1), 69-96.

35. Peng, Z. A.; Peng, X., Formation of High-Quality CdTe, CdSe, and CdS Nanocrystals Using CdO as Precursor. *Journal of the American Chemical Society* **2000,** *123* (1), 183-184.

36. Yu, W. W.; Peng, X., Formation of High-Quality CdS and Other II–VI Semiconductor Nanocrystals in Noncoordinating Solvents: Tunable Reactivity of Monomers. *Angewandte Chemie International Edition* **2002,** *41* (13), 2368-2371.

37. Yu, W. W.; Qu, L.; Guo, W.; Peng, X., Experimental Determination of the Extinction Coefficient of CdTe, CdSe, and CdS Nanocrystals. *Chemistry of Materials* **2003,** *15* (14), 2854-2860.

38. Rivera Gil, P.; Oberdörster, G.; Elder, A.; Puntes, V.; Parak, W. J., Correlating Physico-Chemical with Toxicological Properties of Nanoparticles: The Present and the Future. *ACS Nano* **2010,** *4* (10), 5527-5531.

39. Panthani, M. G.; Akhavan, V.; Goodfellow, B.; Schmidtke, J. P.; Dunn, L.; Dodabalapur, A.; Barbara, P. F.; Korgel, B. A., Synthesis of $CuInS_2$, $CuInSe_2$, and $Cu(In_xGa_{1-x})Se_2$ (CIGS) Nanocrystal "Inks" for Printable Photovoltaics. *Journal of the American Chemical Society* **2008,** *130* (49), 16770-16777.

40. Yue, W.; Han, S.; Peng, R.; Shen, W.; Geng, H.; Wu, F.; Tao, S.; Wang, M., $CuInS_2$ quantum dots synthesized by a solvothermal route and their application as effective electron acceptors for hybrid solar cells. *Journal of Materials Chemistry* **2010,** *20* (35), 7570-7578.

41. Tell, B.; Shay, J. L.; Kasper, H. M., Electrical Properties, Optical Properties, and Band Structure of $CuGaS_2$ and $CuInS_2$. *Physical Review B* **1971,** *4* (8), 2463-2471.

42. Pein, A.; Baghbanzadeh, M.; Rath, T.; Haas, W.; Maier, E.; Amenitsch, H.; Hofer, F.; Kappe, C. O.; Trimmel, G., Investigation of the Formation of $CuInS_2$ Nanoparticles by the Oleylamine Route: Comparison of Microwave-Assisted and Conventional Syntheses. *Inorganic Chemistry* **2010,** *50* (1), 193-200.

43. Arici, E.; Sariciftci, N. S.; Meissner, D., Hybrid Solar Cells Based on Nanoparticles of $CuInS_2$ in Organic Matrices. *Advanced Functional Materials* **2003,** *13* (2), 165-171.

44. Canham, L. T., Silicon quantum wire array fabrication by electrochemical and chemical dissolution of wafers. *Applied Physics Letters* **1990,** *57* (10), 1046-1048.

45. Nassar, N. T.; Barr, R.; Browning, M.; Diao, Z.; Friedlander, E.; Harper, E. M.; Henly, C.; Kavlak, G.; Kwatra, S.; Jun, C.; Warren, S.; Yang, M.-Y.; Graedel, T. E., Criticality of the Geological Copper Family. *Environmental Science & Technology* **2011,** *46* (2), 1071-1078.

46. Inoue, T.; Fujishima, A.; Konishi, S.; Honda, K., Photoelectrocatalytic reduction of carbon dioxide in aqueous suspensions of semiconductor powders. *Nature* **1979,** *277* (5698), 637-638.

47. Shen, F.; Que, W.; He, Y.; Yuan, Y.; Yin, X.; Wang, G., Enhanced Photocatalytic Activity of ZnO Microspheres via Hybridization with $CuInSe_2$ and $CuInS_2$ Nanocrystals. *ACS Applied Materials & Interfaces* **2012,** *4* (8), 4087-4092.

48. Look, D. C.; Manthuruthil, J. C., Electron and hole conductivity in $CuInS_2$. *Journal of Physics and Chemistry of Solids* **1976,** *37* (2), 173-180.

49. Binsma, J. J. M.; Giling, L. J.; Bloem, J., Phase relations in the system Cu_2S-In_2S_3. *Journal of Crystal Growth* **1980,** *50* (2), 429-436.

50. Huang, W.-C.; Tseng, C.-H.; Chang, S.-H.; Tuan, H.-Y.; Chiang, C.-C.; Lyu, L.-M.; Huang, M. H., Solvothermal Synthesis of Zincblende and Wurtzite $CuInS_2$ Nanocrystals and Their Photovoltaic Application. *Langmuir* **2012,** *28* (22), 8496-8501.

51. Zhong, H.; Bai, Z.; Zou, B., Tuning the Luminescence Properties of Colloidal I–III–VI Semiconductor Nanocrystals for Optoelectronics and Biotechnology Applications. *The Journal of Physical Chemistry Letters* **2012,** *3* (21), 3167-3175.

52. Kolny-Olesiak, J.; Weller, H., Synthesis and Application of Colloidal $CuInS_2$ Semiconductor Nanocrystals. *ACS Applied Materials & Interfaces* **2013,** *5* (23), 12221-12237.

53. De Trizio, L.; Prato, M.; Genovese, A.; Casu, A.; Povia, M.; Simonutti, R.; Alcocer, M. J. P.; D'Andrea, C.; Tassone, F.; Manna, L., Strongly Fluorescent Quaternary Cu–In–Zn–S Nanocrystals Prepared from $Cu_{1-x}InS_2$ Nanocrystals by Partial Cation Exchange. *Chemistry of Materials* **2012,** *24* (12), 2400-2406.

54. Shen, X.; Hernández-Pagan, E. A.; Zhou, W.; Puzyrev, Y. S.; Idrobo, J.-C.; Macdonald, J. E.; Pennycook, S. J.; Pantelides, S., T., Interlaced crystals: Perfect Bravais Lattices with interlaced chemical order revealed by real-space crystallography. *In Review* **2014**.

55. Talapin, D. V.; Nelson, J. H.; Shevchenko, E. V.; Aloni, S.; Sadtler, B.; Alivisatos, A. P., Seeded Growth of Highly Luminescent CdSe/CdS Nanoheterostructures with Rod and Tetrapod Morphologies. *Nano Letters* **2007,** *7* (10), 2951-2959.

56. Amirav, L.; Alivisatos, A. P., Luminescence Studies of Individual Quantum Dot Photocatalysts. *Journal of the American Chemical Society* **2013,** *135* (35), 13049-13053.

57. Qi, Y.; Liu, Q.; Tang, K.; Liang, Z.; Ren, Z.; Liu, X., Synthesis and Characterization of Nanostructured Wurtzite $CuInS_2$: A New Cation Disordered Polymorph of $CuInS_2$. *The Journal of Physical Chemistry C* **2009,** *113* (10), 3939-3944.

58. Czekelius, C.; Hilgendorff, M.; Spanhel, L.; Bedja, I.; Lerch, M.; Müller, G.; Bloeck, U.; Su, D.-S.; Giersig, M., A Simple Colloidal Route to Nanocrystalline $ZnO/CuInS_2$ Bilayers. *Advanced Materials* **1999,** *11* (8), 643-646.

59. Shen, X.; Pantelides, S., Electron and Hole Effective Mass of Wurtzite $CuInS_2$. Unpublished Results, **2014**.

60. Yoshino, K.; Ikari, T.; Shirakata, S.; Miyake, H.; Hiramatsu, K., Sharp band edge photoluminescence of high-purity $CuInS_2$ single crystals. *Applied Physics Letters* **2001,** *78* (6), 742.

61. Yakushev, M. V.; Martin, R. W.; Mudryi, A. V., Diamagnetic shifts of free excitons in $CuInS_2$ in magnetic fields. *Applied Physics Letters* **2009,** *94* (4), 0421091-0421093.

62. Brus, L., Electronic wave functions in semiconductor clusters: experiment and theory. *The Journal of Physical Chemistry* **1986,** *90* (12), 2555-2560.

63. Niezgoda, J. S.; Harrison, M. A.; McBride, J. R.; Rosenthal, S. J., Novel Synthesis of Chalcopyrite $Cu_xIn_yS_2$ Quantum Dots with Tunable Localized Surface Plasmon Resonances. *Chemistry of Materials* **2012,** *24* (16), 3294-3298.

64. Castro, S. L.; Bailey, S. G.; Raffaelle, R. P.; Banger, K. K.; Hepp, A. F., Nanocrystalline Chalcopyrite Materials ($CuInS_2$ and $CuInSe_2$) via Low-Temperature Pyrolysis of Molecular Single-Source Precursors. *Chemistry of Materials* **2003,** *15* (16), 3142-3147.

65. Krunks, M.; Bijakina, O.; Varema, T.; Mikli, V.; Mellikov, E., Structural and optical properties of sprayed $CuInS_2$ films. *Thin Solid Films* **1999,** *338* (1–2), 125-130.

66. Courtel, F. M.; Paynter, R. W.; Marsan, B.; Morin, M., Synthesis, Characterization, and Growth Mechanism of n-Type $CuInS_2$ Colloidal Particles. *Chemistry of Materials* **2009,** *21* (16), 3752-3762.

67. Pons, T.; Pic, E.; Lequeux, N.; Cassette, E.; Bezdetnaya, L.; Guillemin, F.; Marchal, F.; Dubertret, B., Cadmium-Free $CuInS_2$/ZnS Quantum Dots for Sentinel Lymph Node Imaging with Reduced Toxicity. *ACS Nano* **2010,** *4* (5), 2531-2538.

68. Deng, D.; Chen, Y.; Cao, J.; Tian, J.; Qian, Z.; Achilefu, S.; Gu, Y., High-Quality $CuInS_2$/ZnS Quantum Dots for In vitro and In vivo Bioimaging. *Chemistry of Materials* **2012,** *24* (15), 3029-3037.

69. Lin, Y.; Zhang, F.; Pan, D.; Li, H.; Lu, Y., Sunlight-driven photodegradation of organic pollutants catalyzed by $TiO_2/(ZnS)_x(CuInS_2)_{1-x}$ nanocomposites. *Journal of Materials Chemistry* **2012,** *22* (18), 8759-8763.

70. Li, L.; Coates, N.; Moses, D., Solution-Processed Inorganic Solar Cell Based on in Situ Synthesis and Film Deposition of $CuInS_2$ Nanocrystals. *Journal of the American Chemical Society* **2009,** *132* (1), 22-23.

71. Koo, B.; Patel, R. N.; Korgel, B. A., Wurtzite−Chalcopyrite Polytypism in $CuInS_2$ Nanodisks. *Chemistry of Materials* **2009,** *21* (9), 1962-1966.

72. Pan, D.; An, L.; Sun, Z.; Hou, W.; Yang, Y.; Yang, Z.; Lu, Y., Synthesis of Cu−In−S Ternary Nanocrystals with Tunable Structure and Composition. *Journal of the American Chemical Society* **2008,** *130* (17), 5620-5621.

73. Grabolle, M.; Spieles, M.; Lesnyak, V.; Gaponik, N.; Eychmüller, A.; Resch-Genger, U., Determination of the Fluorescence Quantum Yield of Quantum Dots: Suitable Procedures and Achievable Uncertainties. *Analytical Chemistry* **2009,** *81* (15), 6285-6294.

74. Brouwer, A. M., Standards for photoluminescence quantum yield measurements in solution (IUPAC Technical Report). *Pure Applied Chemistry* **2011,** *83* (12), 16.

75. Uehara, M.; Watanabe, K.; Tajiri, Y.; Nakamura, H.; Maeda, H., Synthesis of $CuInS_2$ fluorescent nanocrystals and enhancement of fluorescence by controlling crystal defect. *The Journal of Chemical Physics* **2008,** *129* (13), 1347091-1347096.

76. Xie, R.; Rutherford, M.; Peng, X., Formation of High-Quality I−III−VI Semiconductor Nanocrystals by Tuning Relative Reactivity of Cationic Precursors. *Journal of the American Chemical Society* **2009,** *131* (15), 5691-5697.

77. Li, L.; Pandey, A.; Werder, D. J.; Khanal, B. P.; Pietryga, J. M.; Klimov, V. I., Efficient Synthesis of Highly Luminescent Copper Indium Sulfide-Based Core/Shell Nanocrystals with Surprisingly Long-Lived Emission. *Journal of the American Chemical Society* **2011,** *133* (5), 1176-1179.

78. Zhang, W.; Zhong, X., Facile Synthesis of ZnS−$CuInS_2$-Alloyed Nanocrystals for a Color-Tunable Fluorchrome and Photocatalyst. *Inorganic Chemistry* **2011,** *50* (9), 4065-4072.

79. Kruszynska, M.; Borchert, H.; Parisi, J.; Kolny-Olesiak, J., Synthesis and Shape Control of $CuInS_2$ Nanoparticles. *Journal of the American Chemical Society* **2010,** *132* (45), 15976-15986.

80. Dethlefsen, J. R.; Døssing, A., Preparation of a ZnS Shell on CdSe Quantum Dots Using a Single-Molecular ZnS Precursor. *Nano Letters* **2011,** *11* (5), 1964-1969.

81. Batabyal, S. K.; Tian, L.; Venkatram, N.; Ji, W.; Vittal, J. J., Phase-Selective Synthesis of $CuInS_2$ Nanocrystals. *The Journal of Physical Chemistry C* **2009,** *113* (33), 15037-15042.

82. Langford, J. I.; Wilson, A. J. C., Scherrer after sixty years: A survey and some new results in the determination of crystallite size. *Journal of Applied Crystallography* **1978,** *11* (2), 102-113.

83. Ungár, T., The Meaning of Size Obtained from Broadened X-ray Diffraction Peaks. *Advanced Engineering Materials* **2003,** *5* (5), 323-329.

84. Omata, T.; Nose, K.; Otsuka-Yao-Matsuo, S., Size dependent optical band gap of ternary I-III-VI_2 semiconductor nanocrystals. *Journal of Applied Physics* **2009,** *105* (7), 0731061-0731065.

85. Zhang, Q.; Xie, J.; Yang, J.; Lee, J. Y., Monodisperse Icosahedral Ag, Au, and Pd Nanoparticles: Size Control Strategy and Superlattice Formation. *ACS Nano* **2008,** *3* (1), 139-148.

86. Smith, D. K.; Luther, J. M.; Semonin, O. E.; Nozik, A. J.; Beard, M. C., Tuning the Synthesis of Ternary Lead Chalcogenide Quantum Dots by Balancing Precursor Reactivity. *ACS Nano* **2010,** *5* (1), 183-190.

87. Kongkanand, A.; Tvrdy, K.; Takechi, K.; Kuno, M.; Kamat, P. V., Quantum Dot Solar Cells. Tuning Photoresponse through Size and Shape Control of CdSe−TiO_2 Architecture. *Journal of the American Chemical Society* **2008,** *130* (12), 4007-4015.

88. Hines, M. A.; Guyot-Sionnest, P., Synthesis and Characterization of Strongly Luminescing ZnS-Capped CdSe Nanocrystals. *The Journal of Physical Chemistry* **1996,** *100* (2), 468-471.

89. Nicolau, Y. F., Solution deposition of thin solid compound films by a successive ionic-layer adsorption and reaction process. *Applications of Surface Science* **1985,** *22–23, Part 2* (0), 1061-1074.

90. Yoe, J.; Overholser, L., Reactivity of Substituted Thioureas with Inorganic Ions. *Industrial & Engineering Chemistry Analytical Edition* **1942,** *14* (5), 435-437.

91. Hancock, R. D.; Martell, A. E., Hard and Soft Acid-Base Behavior in Aqueous Solution: Steric Effects Make Some Metal Ions Hard: A Quantitative Scale of Hardness-Softness for Acids and Bases. *Journal of Chemical Education* **1996,** *73* (7), 654.

92. Tauc, J.; Grigorovici, R.; Vancu, A., Optical Properties and Electronic Structure of Amorphous Germanium. *physica status solidi (b)* **1966,** *15* (2), 627-637.

93. Lu, X.; Zhuang, Z.; Peng, Q.; Li, Y., Wurtzite Cu_2ZnSnS_4 nanocrystals: a novel quaternary semiconductor. *Chemical Communications* **2011,** *47* (11), 3141-3143.

94. Chen, B.; Zhong, H.; Zhang, W.; Tan, Z. a.; Li, Y.; Yu, C.; Zhai, T.; Bando, Y.; Yang, S.; Zou, B., Highly Emissive and Color-Tunable $CuInS_2$-Based Colloidal Semiconductor Nanocrystals: Off-Stoichiometry Effects and Improved Electroluminescence Performance. *Advanced Functional Materials* **2012,** *22* (10), 2081-2088.

95. Castro, S. L.; Bailey, S. G.; Raffaelle, R. P.; Banger, K. K.; Hepp, A. F., Synthesis and Characterization of Colloidal $CuInS_2$ Nanoparticles from a Molecular Single-Source Precursor. *The Journal of Physical Chemistry B* **2004,** *108* (33), 12429-12435.

96. Binsma, J. J. M.; Giling, L. J.; Bloem, J., Luminescence of $CuInS_2$: I. The broad band emission and its dependence on the defect chemistry. *Journal of Luminescence* **1982,** *27* (1), 35-53.

97. Binsma, J. J. M.; Giling, L. J.; Bloem, J., Luminescence of $CuInS_2$: II. Exciton and near edge emission. *Journal of Luminescence* **1982,** *27* (1), 55-72.

98. Krustok, J.; Raudoja, J.; Schön, J. H.; Yakushev, M.; Collan, H., The role of deep donor–deep acceptor complexes in CIS-related compounds. *Thin Solid Films* **2000,** *361–362* (0), 406-410.

99. Hamanaka, Y.; Kuzuya, T.; Sofue, T.; Kino, T.; Ito, K.; Sumiyama, K., Defect-induced photoluminescence and third-order nonlinear optical response of chemically synthesized chalcopyrite $CuInS_2$ nanoparticles. *Chemical Physics Letters* **2008,** *466* (4–6), 176-180.